TÉCNICO LISBOA

Accuracy Evaluation in Robot-Assisted and Ultrasound-Guided Neurosurgery

Pedro Veigas dos Santos

Thesis to obtain the Master of Science Degree in

Mechanical Engineering

Supervisors: Prof. Jorge Manuel Mateus Martins
Dr. Manuel Herculano Carvalho

Examination Committee

Chairperson: Prof. Carlos Cardeira
Supervisor: Prof. Jorge Manuel Mateus Martins
Member of the Committee: Prof. João Miguel Sanches

January 2021

Acknowledgments

Through the last several years, Instituto Superior Técnico has been my second home. As an high school student, it was always my intention to graduate in this institution and I can say that I am really glad it went that way. I would like to express my deepest thanks for everything I have learned here. It not only made me an engineer, but also, surely, made me a better and stronger person.

I would also like to thank Professor Jorge Martins for the opportunity to work on this project, at the Surgical Robotics Laboratory, and for the invaluable guidance provided. His capacity to motivate me and to clarify my issues and doubts was remarkable ever since this journey started.

A special thanks must also be given to my colleague João Oliveira. I really can't thank him enough for all the patience, and for all the time spent teaching me how to work with every tool inside the laboratory. Also, thanks for every discussion about science and engineering, and for making me justify any idea that came to my mind. It is fair to say that without his help, this thesis would not be nowhere near what it is.

I must express my most sincere gratitude to my family for the unconditional support and comprehension. To my mother for her ceaseless belief in my capabilities and to my father for his outstanding availability.

To my girlfriend, I must also express my most sincere gratitude. The support you gave me through the past years has been incredible. Thank you for all the advice and for always being there for me. Most of all, thank you for all the love, and friendship.

I must also thank the FST 08e and FST 09e team members, which I had the huge pleasure of work with, and certainly taught me a lot.

Lastly, but definitely not least, a huge thanks must also be given to my friends which travelled this long path side by side with me. Completing a degree in IST is much easier when we have the right people next to us. I must give a special thanks to João Rego, who is the greatest expert in 3D printing I know, for building every single component I designed to accomplish this work, and to Carolina Barata for her photographer skills.

Resumo

O campo da neurocirurgia é conhecido por exigir um elevado nível de exatidão associado a cada procedimento realizado. Por outro lado, os recentes desenvolvimentos na área da interação humano-robô possibilitaram o aparecimento de sistemas cirúrgicos de controlo partilhado, nos quais cabe ao cirurgião tomar cada decisão, enquanto que, ao robô, cabe a correção do erro humano, associado à ação do médico.

Neste trabalho, é proposto um sistema de neuronavegação baseado no robô LBR Med, desenvolvido pela empresa KUKA. Será, assim, feita uma avaliação do erro associado à utilização do dito sistema, especialmente no que diz respeito às etapas de registo intraoperatório e de posicionamento da agulha, bem como das causas do mesmo.

A avaliação deste sistema será realizada em ambiente laboratorial, simulando os procedimentos de neurocirurgia, com a utilização de um fantoma antropomórfico capaz de simular o crânio e o interior do cérebro do paciente.

Dito isto, será realizado um registo intraoperatório com recurso a imagens de ultrassons e de TAC. Assim, o método proposto é considerado não-invasivo e contorna alguns dos mais importantes inconvenientes associados às tecnologias utilizadas atualmente. É ainda de referir que todos os aspectos associados a esta etapa serão estudados, nomeadamente, a calibração do ecógrafo, a segmentação das imagens de ambas as modalidades, e os algoritmos de registo rígido. Por fim, no que diz respeito ao posicionamento da agulha, a performance do robô será avaliada utilizando o sistema de navegação Polaris Spectra, desenvolvido pela empresa Northern Digital.

Palavras-chave: Neuronavegação, LBR Med, Ultrassons, Segmentação, Registo

Abstract

The neurosurgery field demands an high level of accuracy and precision associated to each performed procedure. On the other hand, the recent developments in the human-robot area allowed the rise of surgical shared control systems. In these, the surgeon is responsible for every decision, while the robot is responsible for correcting the human error associated do the surgeon's action.

In this work a neuronavigation system based on the LBR Med robot, developed by KUKA, is proposed. Furthermore, an error evaluation will be performed to assess the performance of such system, concerning the intra-operative registration and the needle placement stages. By doing so, the most important sources of inaccuracy will be determined.

Such evaluation will be performed in the laboratory, in a simulated neurosurgical environment, using an antropomorphic phantom to recreate the patient's cranium and brain.

The intraoperative registration will be performed by means of CT and ultrasound images. Thus, the proposed method is a non-invasive one and overcomes the most important drawbacks associated with the state-of-the-art technologies. It is also important to refer that every aspect regarding this stage will be addressed, such as, the ultrasound calibration, the images segmentation and the rigid registration algorithms. Finally, in what concerns the needle positioning, the robot performance will be evaluated using the navigation system Polaris Spectra, developed by Northern Digital.

Keywords: Neuronavigation, LBR Med, Ultrasound Imaging, Segmentation, Registration

Contents

List of Tables

List of Figures

Nomenclature

Greek symbols

μ	Mean.
σ	Standard Deviation.

Roman symbols

${}^{CT}s$	Size of a CT voxel.
${}^{US}s$	Size of an ultrasound pixel.
e_p	Position error.
e_v	Orientation error.
$k_1,\ k_2$	Principal Curvatures.
K_G	Gauss Curvature.
K_H	Mean Curvature.
p	Point in Homogeneous coordinates.
p_A^B	Position of the point A expressed in the coordinate system B.
px	Pixel.
R	Rotation matrix in Cartesian coordinates.
T	Transformation matrix in Homogeneous coordinates.
t	Translation vector in Cartesian coordinates.
T_A^B	Transformation from the coordinate system A to coordinate system B.
v	Vector in Homogeneous coordinates.
v_A^B	Orientation of the vector A expressed in the coordinate system B.
vx	Voxel.
$X,\ Y,\ Z$	Cartesian Axes.

x, y, z Cartesian components.

Superscripts

T Transpose.

Glossary

2D	Two-dimensional.
3D	Three-dimensional.
CR	Calibration Reproducibility.
CT	Computed Tomography.
HU	Hounsfield Units.
ICP	Iterative Closest Point.
IGT	Image-Guided Therapy.
IST	Instituto Superior Técnico.
MHA	MetaImage medical format.
MRI	Magnetic Ressonance Imaging.
NDI	Northern Digital.
PCA	Principal Component Analysis.
PET	Positron Emission Tomography.
PLUS	Public Software Library for Ultrasound.
PRA	Point Reconstruction Accuracy.
RANSAC	Random Sample Consensus.
SRL	Surgical Robotics Laboratory.
TRE	Target Registration Error.
US	Ultrasound.
XML	Extensible Markup Language.

Chapter 1

Introduction

1.1 Motivation

Throughout the past few decades, a huge effort has been put into the development and improvement of the surgical navigation technology, allowing the surgical procedures to be performed in a less invasive manner and still assuring the requirements of high precision and accuracy.

Consequently, several projects have been developed in this field by the students in the Surgical Robotics Laboratory at Instituto Superior Técnico, of which, the works done by Elyseu [1], which studied the intraoperative registration, and Ferreira [2], which focused on image-guided pedicle screw placement, are of particular importance.

On the other hand, the surgical robotics field has also been getting more attention, given the ability of robots to compensate the human shortcomings, specially in what concerns precision, concentration and endurance. Motivated by this, there is the study of the position and force control of a lightweight robot for orthopedic surgery, done by Pires [3], and more recently the integration of the KUKA LBR Med in the neurosurgical framework by Oliveira [4], which focused on the evaluation of the robot control laws and the implementation of a suitable communication protocol. Furthermore, the promising results achieved in [4] are the cornerstone for the present work.

Therefore, it is left to perform a quantitative analysis of the system's accuracy which is crucial to conclude about the viability of using it for neurosurgical applications.

1.2 Objectives

The present work aims to achieve three principal objectives.

The most important is the study of the image-to-patient registration problem in neurosurgery using intraoperative ultrasound and preoperative CT imaging. Every aspect regarding this problem is aimed to be covered. This includes the ultrasound calibration, both the CT and the ultrasound images segmentation and the rigid registration algorithms.

Secondly, there is the development of a systematic stepwise evaluation method that can be used to

determine sources of inaccuracy and assess the error propagation in a robotic neuronavigation system in a quantitative manner.

Finally, to apply the aforementioned objectives using the KUKA LBR Med and an anthropomorphic cranial phantom, in the laboratory, simulating a surgical environment, so to evaluate the system's performance.

1.3 Thesis Outline

The present document is divided into six chapters. The **second chapter** presents an overview about the topic, this aims to provide the adequate background knowledge to the reader so that the present work can be fully understood. It starts by describing how the neurosurgery has evolved and how it is performed nowadays, presenting a review about the existing systems and techniques. Then it focuses on how the robotic systems can be integrated in this field describing the main advantages of these, and afterwards, a brief description about the used imaging modalities is made. It ends by describing in detail the proposed neuronavigation solution.

The **third chapter** aims to introduce every piece of software and hardware used, explaining the role of each. Also, it presents the work methodology, which describes the experiments performed throughout this work. It aims to introduce the important variables and data, how these were acquired or determined and to describe how the quality assessment was performed. By doing so, every development presented in the **fourth chapter** will come up justified.

The **fourth chapter** presents a detailed description of every implementation, justifying the choices and assumptions made. This is divided into three main sections. Firstly, there is presented the image acquisition and treatment and the segmentation techniques, then the setup calibration, and finally the registration techniques employed.

The **fifth chapter** presents the results of every experiment described in the methodology section applying the techniques described in the **fourth chapter**. Subsequently, a discussion is presented to justify the results presented.

Finally, in the **sixth chapter** one will present a qualitative evaluation of the results. By doing so, it will be possible to take conclusions on whether or not the right choices were made and about the viability of the proposed neuronavigation system. Finally, the most important future developments will be addressed.

Chapter 2

Background

2.1 Brain Biopsy

A brain biopsy is a surgical intervention that aims to extract a small piece of brain tissue for the diagnosis of abnormalities. Furthermore, such abnormalities can be located in the surface of the brain or deep in it.

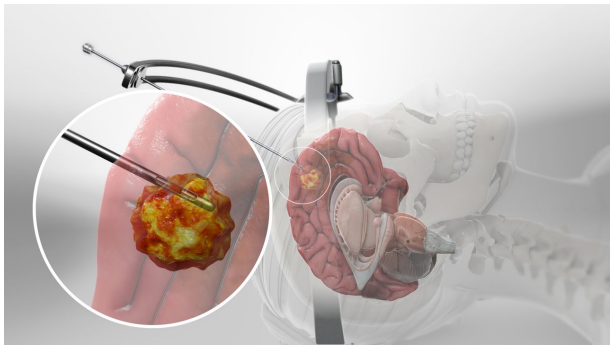

Figure 2.1: Brain Biopsy. (From [5])

To collect the sample, a probe (or needle) is used as shown in figure 2.1. Also, due to the sensitive nature of the brain, this is a very invasive procedure and the path travelled by the probe, until it reaches the target, must be carefully planned. Finally, a brain biopsy can be classified as open biopsy, if the brain tissue is exposed through a craniotomy, i.e., the temporary removal a portion of the skull, or as closed biopsy, if only a small hole is drilled in the skull.

The present work focuses on the closed biopsy procedure. This is a less invasive methodology but requires the employment of the stereotactic frame or a neuronavigation system, section 2.2, to achieve the required performance.

2.2 Neuronavigation

2.2.1 Historical Perspective

Although the first known documentation about surgical interventions on human cranium are from the neolithic period, the modern neurological surgery, as it is described today, only exists since the ending of XIX century. It was in 1879 that the Scottish surgeon William Macewen performed the first successful brain tumour removal. It is however to Victor Horsley, surgeon of the National Hospital of Queens Square in London, that the title ”Father of Neurosurgery” is attributed on account of the several intracranial interventions that he has performed. Also, it is important to refer the work of Harvey Cushing, who created several techniques and methods that allowed these interventions to be done safely on humans.

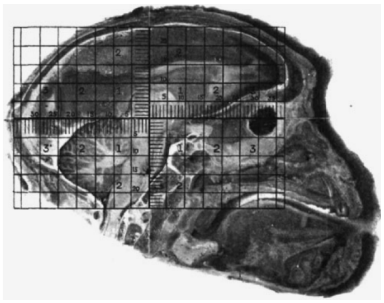

Figure 2.2: Horlsey and Clarke experiments illustration. (From [6])

The important concept of stereotaxy was introduced in 1908 by Victor Horsley and the engineer Robert H. Clark. Their experiments aimed to locate deep brain structures in a three-dimensional coordinate system using external cranial references, figure 2.2. They verified that such procedure was not sufficiently accurate to be performed on humans and the concept of stereotaxy was abandoned by neurosurgeons until the emergence of the imaging modalities capable of increasing the method’s accuracy.

(a) Pneumoencephalography

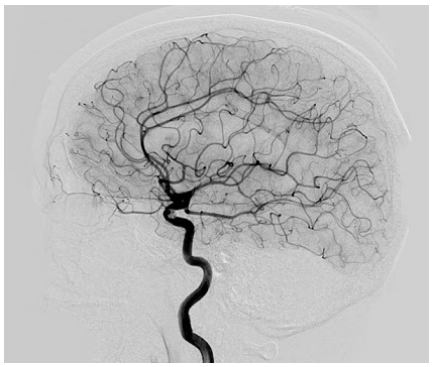

(b) Angiography

Figure 2.3: Primordial imaging modalities.

The X-radiation was discovered by Wilhelm Röntgen in 1895 and made it possible for Walter Dandy to invent the ventriculography in 1918 and improve it to create the pneumoencephalography in 1919. The method consisted in draining the most of the cerebrospinal fluid from around the brain replacing it

with air to allow the structure of the brain to clearly show up on an X-ray image, figure 2.3a. Also, in 1927 the Portuguese neurologist Egas Moniz developed the angiography which allowed to image the blood vessels in and around the brain, figure 2.3b, thereby allowing the detection of abnormalities.

The appearance of the aforementioned imaging modalities allowed the stereotaxy to be considered again and led the first stereotactic apparatus to be invented in 1947 by E. A. Spiegel and H. T. Wycis. Such instrument allowed a probe to be positioned in a three-dimensional cartesian coordinate system which was overlaid to the pneumoencephalography images.

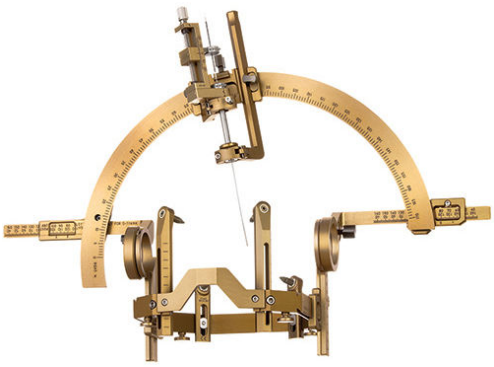

Figure 2.4: Leksell Stereotactic System® (From [7])

In 1949 Lars Leksell developed a new instrument, figure 2.4. This was the first stereotactic system to employ the ”center-of-arc” principle, and used three polar coordinates: angle, depth and anterior-posterior location, contrasting with the cartesian coordinate system of the Spiegel-Wycis device. This new device represented a considerable improvement since it provided maximum flexibility in choosing the probe entry point and trajectory.

The Leksell stereotactic device has been improved throughout the years and it is still used today. Furthermore, the surgical interventions that use an apparatus like this are called frame-based sterotactic surgeries.

(a) CT

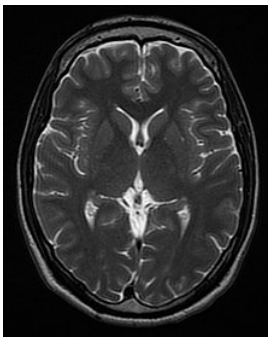

(b) MRI

Figure 2.5: Modern imaging modalities.

By the 1970’s two new image modalities emerged which made it possible to directly observe the

brain structures in a volume, providing valuable information to the surgeons. On one hand, there is Computed Tomography (CT) invented by G. Hounsfield, figure 2.5a. A CT volume is built by stacking up several slices. On their turn, each slice is the result of multiple X-ray measurements taken from different angles. On the other hand, the Magnetic Ressonance Imaging (MRI), figure 2.5b, was the result of the work developed by Damadian in 1971 and the work developed by Lauterbur as well as Mansfield and Grannell in 1973. This imaging modality uses strong magnetic fields instead of X-rays and the resulting images show a much higher definition in soft tissue contrast than the one found in the CT.

Finally, the ever-increasing capabilities of digital storage, the computer-graphic modelling and manipulation as well as the three-dimensional localization technologies that appeared at end of the XX century empowered the concept of frameless stereotactic surgery, also known as neuronavigation, to arise. The presented historical perspective had, as a principal source of information, the work in [8].

Nowadays, both the frame-based surgery and the neuronavigation are valid options, as both can provide an high accuracy. Therefore, it is the doctor's job to choose between those for each specific case.

2.2.2 Surgical Procedure

The first step in a frameless stereotactic surgery is the acquisition of the preoperative images. Both CT and MRI are usually used and they must be merged resulting in a mixed image space where the doctor can define the target point in the patient's brain and the desired trajectory to reach it.

The surgical room is illustrated in figure 2.7. Here, it is crucial to fix the patient's head so it does not move during the procedure. By doing so, a steady coordinate correspondence between the surgical space and the image space is assured. Such task is accomplished with the Mayfield clamp, a three point fixture mechanism which is screwed to the patients head, figure 2.6.

Figure 2.6: MAYFIELD® Skull Clamp (From [9])

The registration step aims to calculate the aforementioned coordinate transformation and it is described in detail in the next section. This is one of the main focuses of the present work and its importance for the success of the intervention is extreme.

Once the registration is performed, the position of any surgical tool marked with a reflective adaptor in the surgical space can be seen, in the screen, in the image space in real time. This way the tools can be moved relative to the patient's head, based on the CT-MRI images information.

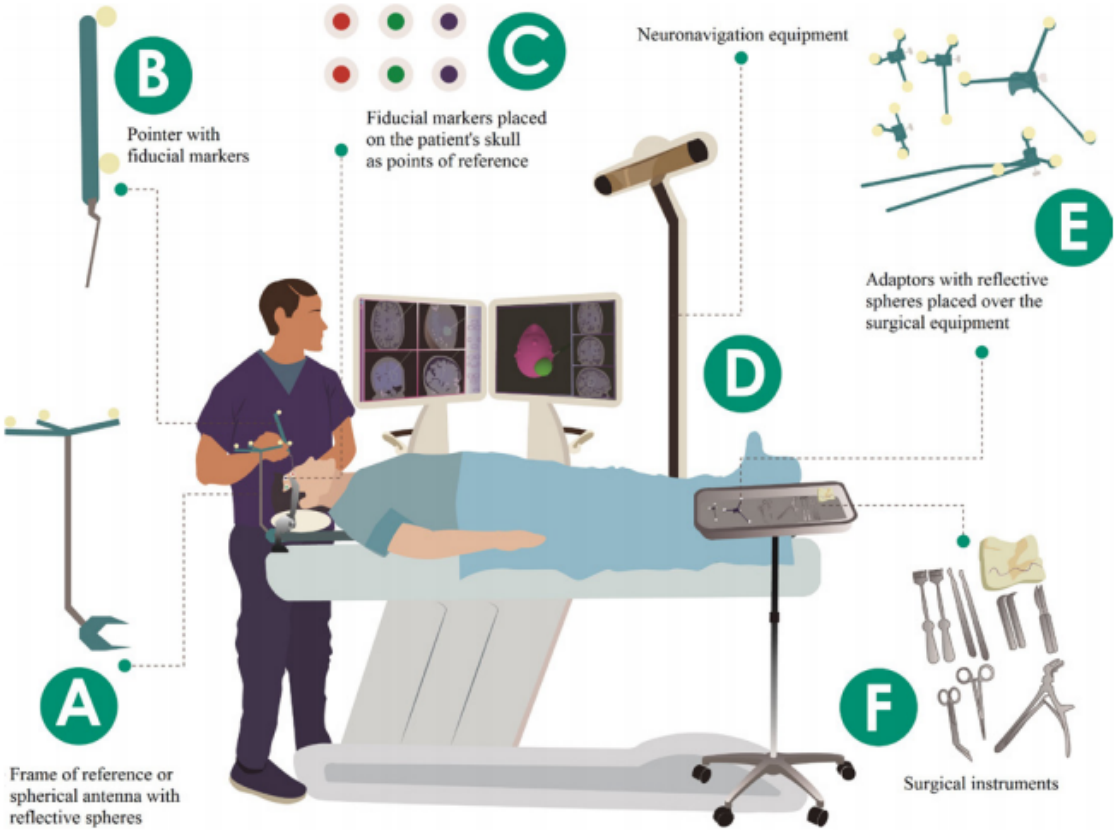

Figure 2.7: The neuronavigation system is composed by a frame of reference (A), attached to the stretcher or to the mayfield clamp, used to detect any undesired movement. A pointer (B) and fiducial markers (C) equipped with reflective spheres that can be detected by the neuronavigation equipment (D). This consists of two light emitters that perform three-dimensional localization trough triangulation. Also a set of screens are available where the doctor can visualize the preoperative images and the position of the surgical tools (F) when equipped with the respective adaptor (E). (From [10])

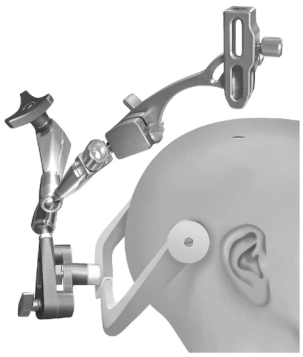

Figure 2.8: Vertek® articulating arm attached to the Mayfield clamp. (From [11])

Finally, the surgeon identifies the entry point and an articulating arm is used to correctly define the needle orientation. Then, the articulating arm degrees of freedom are constrained allowing the needle to move only in depth along the defined path. This movement is controlled by the doctor, and can be monitored with the navigation equipment.

2.2.3 Registration

The process of estimating the coordinate transformation between two reference frames is called registration. The image-to-image registration can be used to merge the CT and MRI or PET (Positron Emission Tomography) images creating a mixed image space, [12, 13]. However, this is out of the scope of this work and one will focus on the image-to-patient registration.

The image-to-patient registration consists in the estimation of a rigid coordinate transformation. This estimation will have as input the CT-MRI images and information acquired in the physical space.

The registration techniques can be divided in two groups, these are the point-pair matching and the surface matching techniques, [14], given that each technique has its advantages and drawbacks.

Point-Pair Matching

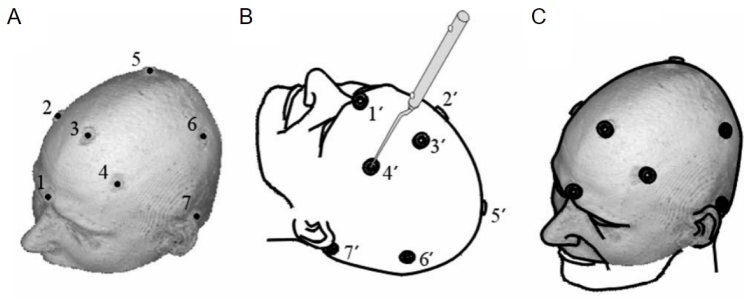

Figure 2.9: Point-Pair registration illustration. Selected fiducials in the image space, A. Fiducials position acquisition in the surgical space, B. Resulting image-to-patient registration , C. (Adapted from [14])

A rigid transformation between two reference frames can be accomplished using 3 or more pairs of non collinear points. These points will be called fiducials and the point-pair matching technique can be subdivided based on the nature of the fiducials used.

On one hand, there is the registration based on natural fiducials. In this technique, the registration is performed using anatomical points of the patient's head that are easy to identify in both the image and the physical spaces, like the edges of the eyes or the nose tip, for example, [15].

On the other hand, the registration can be performed based on artificial fiducials. These are markers that can be glued to the patient's head skin or rigidly fixed to the bone through a previous surgery, [15], and that are specially designed to be easily identified in the images.

Regarding the positive and negative aspects of this methodology, the use of natural fiducials is a non-invasive technique of which the simplicity is the main advantage. On the other hand, the selection of correspondent anatomical points in the image and in the physical space may be difficult and ambiguous. As for the use of artificial markers, the first drawback is the need of an additional CT scanning, after the markers placement, exposing the patient to an additional amount of radiation. The glued markers have the additional drawback of moving due to the skin mobility. The rigidly attached markers do not have this problem making this a very accurate method, however, this technique is very invasive and uncomfortable for the patient.

Surface Matching

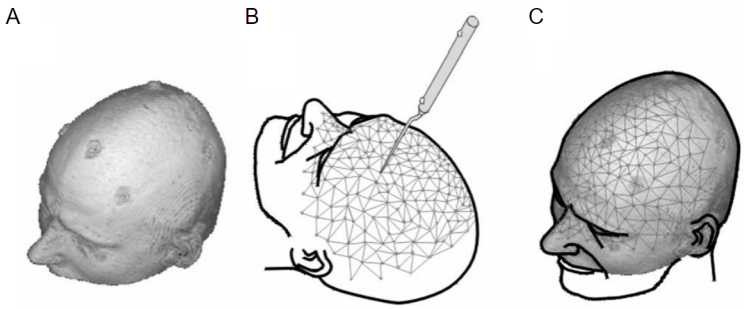

Figure 2.10: Surface matching registration. Segmented surface in the image space, A. Surface acquisition in the surgical space, B. Resulting image-to-patient registration , C. (Adapted from [14])

In the surface matching registration, instead of a set of points with known correspondences, a surface which defines the patient's cranium or skin is used. This surface is extracted from the image space by software. On the other hand, its acquisition in the physical space is performed by the doctor using a pointer, [16], or a laser scanner, [17]. A suitable algorithm must then be employed to estimate the coordinate transformation that best aligns both surfaces.

Comparing the surface matching technique, as it is done nowadays, with point-pair matching methods, this has the advantage of being non-invasive and discarding the need of the additional CT scanning. However, the surface acquisition is still prone to errors due to the skin movement. In order to solve this issue, an innovative method proposes the use of intraoperative ultrasound imaging to acquire the bone surface directly, [1, 18, 19]. Furthermore, this is the technique proposed in the present work.

Error Evaluation

To evaluate the registration quality, Fitzpatrick et al. [20] proposes the taget registration error, TRE. This consists in evaluating the error in the estimation of target points, i.e., the euclidean distance between the real position of a target and the one estimated through the registered image space. The TRE is given by 2.1, where r_i and r'_i are, respectively, the real and the estimated position of each of the N target points.

$$TRE = \frac{1}{N}\sum_{i=1}^{N}\|r_i - r'_i\| \tag{2.1}$$

2.2.4 State of the Art Performance

In this section a review of the reported neuronavigation systems performance is presented.

Strong et al. [21] compares three of the most widely used neuronavigation systems, these are, the Medtronic StealthStation, the BrainLab VectorVision and the Voxim from IVS Solutions. They studied four cadaveric heads and the registration was performed by means of rigidly fixed fiducial markers. They reported a mean TRE ranging from 1-1.5 mm.

The BrainLab system offers the possibility of using a laser scanner to perform a surface matching registration, the Z-touch. This system was tested by Lübbers et al. [22]. In this study, a synthetic human skull model was used and the reported TRE when using this system ranged from 1-1.2 mm. However, the use of a phantom with no skin may cause this result to be unrealistic.

Also interesting is the work of Stieglitz et al. [23] which, through a literature review, reported errors ranging from submillimetric to around 6 mm. Both the point-pair and surface matching techniques were covered and besides the aforementioned systems, this work also includes the FARO Surgicom and the Stryker Navigation System among others. This work also performs an interesting quantification about the accuracy decrease after the registration step, identifying its most prominent origins.

Finally, a previous study performed in the Surgical Robotics Laboratory at IST presented an error evaluation in a neuronavigation procedure [24], and reported an mean TRE of 3.93 mm after te mechanical execution with the Vertek articulating arm.

2.3 Robotics in Neurosurgery

Regarding its technical classification, the robotic systems used in a surgical environment are divided in three classes. These are the supervised controlled systems, the telesurgical systems and the shared control systems, [25].

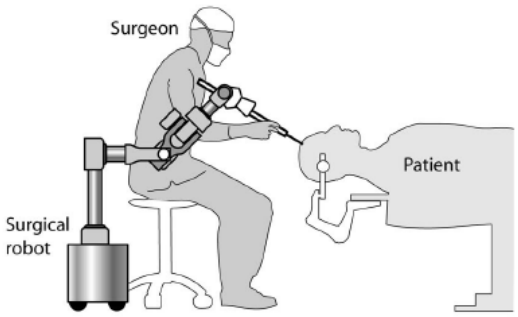

Figure 2.11: Shared control system. (Adapted from [25])

In a supervised controlled system, the surgery is planned by the surgeon in the preoperative stage. These plans are then uploaded to the robot controller and the robot executes the operation autonomously under the supervision of the surgeon.

In a telesurgical system, the robot is controlled by the surgeon by means of an haptic interface. It faithfully replicates the surgeons motions.

Finally, in a shared control system, the surgeon and the robot share the control over the surgical tools. In these systems, the surgeon is responsible for manually guiding the tools and the robot is responsible for providing steady-hand manipulation. This is the most prominent type of robotic systems in neurosurgery and moreover, the system proposed in the present work falls into this category. Figure 2.11 shows a representation of this type of systems.

Nathoo et al. [25] also presents several advantages of using a robotic system in neurosurgery. From those, it is worth stressing the ability to actively constrain the tools to a particular path or position, even

against externally imposed forces, the ability to perform repetitive motions and to hold in a specified position for long periods without tremor and the high accuracy and precision that these systems provide.

(a) NeuroMate® (From [26])

(b) ROSA ONE® (From [27])

Figure 2.12: Robotic Systems.

The first robot used to hold a needle in a brain biopsy was the PUMA 200. This was a standard industrial robot and operated as a supervised controlled system. Nowadays, several robotic systems are available to perform this kind of procedure:

- **ROSA ONE**: This was designed to perform deep brain stimulation and needle placement in a brain biopsy and it is prepared to work with CT and MRI images. Furthermore, the system works under co-manipulation in a frame-based or frameless setup. To perform the image-to-patient registration, it offers the possibility of coupling it with a precise optical distance sensor. Recent studies report an application accuracy of around 4 mm, [28], using the ROSA in a real clinical scenario. This robot is shown in figure 2.12b.

- **Neuromate**: The Neuromate works in similar fashion as ROSA ONE. It can also be used in a frame-based or frameless setup and performs the image-to-patient registration using ultrasonic technology. A set of ultrasonic receivers is attached to the patient's skull while the emitter is mounted on the robot's arm. Different from the previous system, this is a tele-manipulated robot. A phantom based study performed with this, reported an application accuracy of 1.29 mm, [29]. This robot is shown in figure 2.12a.

- **NeuroArm**: This is composed by two seven degree of freedom robotic arms, a system controller and a set of haptic devices. A huge difference between this and the remaining robots is that the NeuroArm is fully MRI compatible, meaning that it can operate inside an MRI scanner. Thus, it allows a real-time update of the brain's position.

2.4 Image Modalities

2.4.1 Ultrasound Imaging

To start with there is the ultrasound imaging. An ultrasound probe is composed of piezoelectric crystals which deform when a voltage is applied. This effect can be used to generate a vibration which in turn produces a sound wave. Conversely, when hit with a sound wave, they undergo a mechanical tension which will deform them, generating a voltage.

When a sound wave is emitted it travels with a speed that is imposed by the physical medium. From there, a series of mechanisms will cause the wave attenuation, being that, the most important one in terms of image formation is the reflection. Every time the sound wave crosses the border between two media with different acoustic impedance, a portion of the energy that it carries is absorbed by the new medium and the remaining is reflected. Moreover, the greater the impedance variation, the more the energy that is reflected, equation 2.2.

$$\alpha_R = \left(\frac{Z_2 - Z_1}{Z_2 + Z_1} \right)^2 \tag{2.2}$$

In this, α_R is the reflection coefficient, and Z_1 and Z_2 are the acoustic impedance of the two media. To create an ultrasound image, a voltage pulse is initially applied to the piezoelectric crystals. The ultrasound wave emitted will be reflected in every media interface and the reflected waves will hit the piezoelectric crystals, generating in turn a voltage. By acquiring this, it is possible to map the space that the ultrasound wave travelled. This process is shown in figure 2.13.

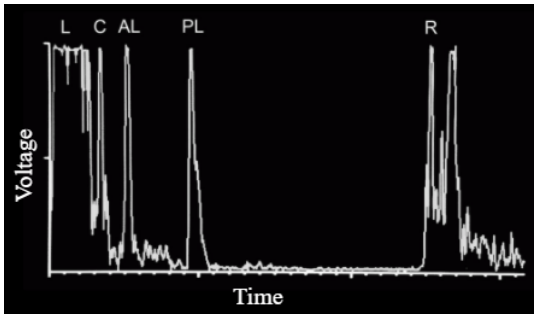

Figure 2.13: A-mode scan in ophthalmic ultrasound diagnostic. Peaks correspond to eyelid (L), cornea (C), anterior (AL), and posterior lens (PL) surfaces and retina (R). (Adapted from [30])

To estimate the depth through a temporal measurement, the speed of sound assumed by most of the ultrasound systems is the mean value for soft tissues, i.e, 1540 m/s. [31]

The first ultrasound probes used only one piezoelectric element. These provided a one-dimensional measurement like the one in figure 2.13 and this technique is called A-mode ultrasound. To build a 2D image, an array of piezoelectric elements is used. And the image is built from a set of A-mode signals. This is called B-mode ultrasound.

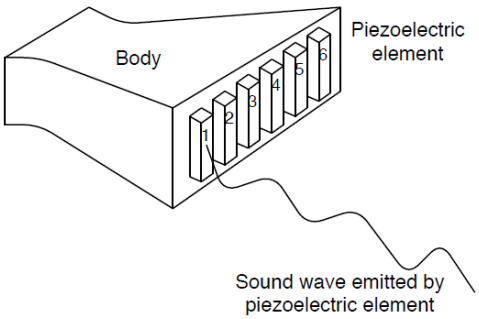

Figure 2.14: B-mode ultrasound. (From [4])

2.4.2 Computed Tomography

The basic principle behind the computed tomography imaging is simple. An X-ray beam is emitted, with an intensity I_0, while a radiation detector is placed on the other side of the patient so that it measures the attenuated radiation I. If the patient's body is composed of n regions with different attenuation coefficients λ_i and lengths l_i, the attenuated beam intensity can be calculated through 2.3.

$$I = I_0 \cdot e^{-\sum_{i=1}^{n} \lambda_i l_i} \tag{2.3}$$

Building the image consists in determining the value of each λ_i and l_i. With a single transmission measurement, too many unknowns exist and a solution can not be found. However, if several measurements are taken with different orientations, it becomes possible to solve the set of resulting equations, employing a suitable algorithm, [32], and map the interior of the patient's body. Figure 2.15, shows a very clear schematic representation of how this process works.

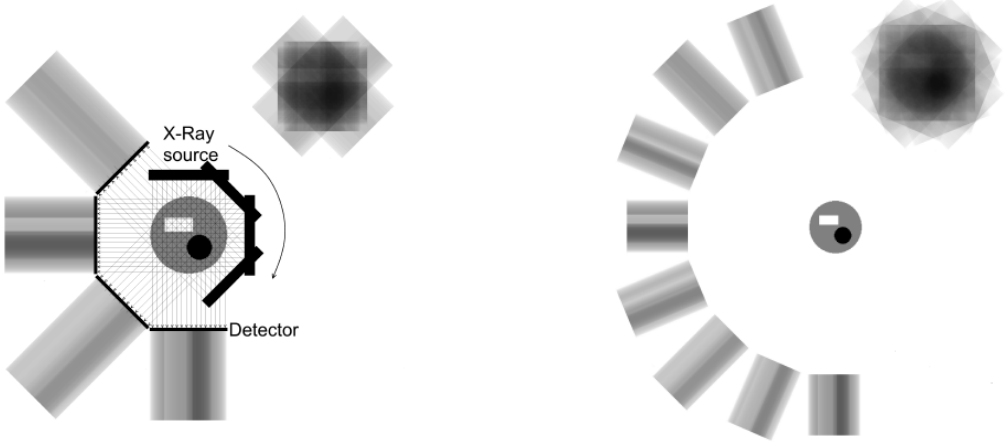

(a) (b)

Figure 2.15: Image formation. Views evaluated at 45 degrees steps over the object (a). Views evaluated at 22.5 degrees steps over the object (b). (Adapted from [33])

To build the CT volume, a set of these images is acquired, in different axial planes, and stacked up. Finally, the attenuation coefficients are normalized through the Hounsfield Units (HU). This is accomplished through equation 2.4.

$$HU = \frac{\lambda - \lambda_{water}}{\lambda_{water} - \lambda_{air}} \cdot 1000 \tag{2.4}$$

Where λ_{water} and λ_{air} are respectively the attenuation coefficients of the water and air. The HU values for human body range from -1000 to 3000.

2.5 Proposed Project

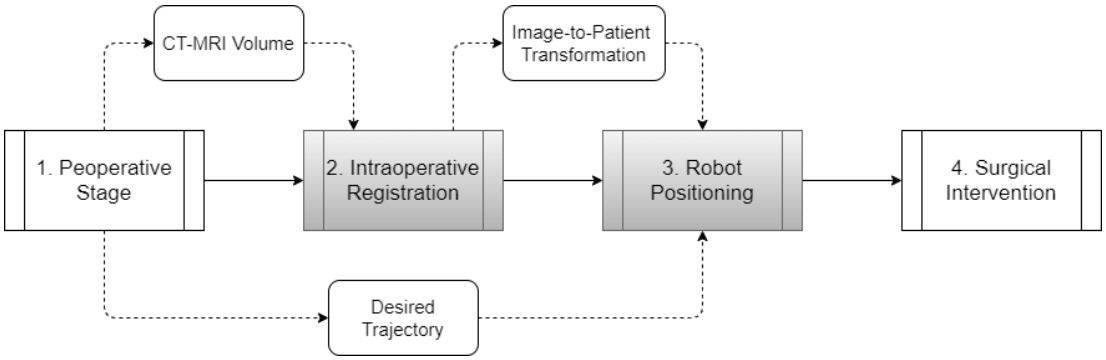

Figure 2.16: Surgical Procedure Stages.

The project presented in this thesis proposes a robot-assisted neuronavigation system in a shared control fashion which disregards the use of any additional 3D localization technology in the surgical room. In order to provide a better understanding, let the neurosurgical procedure be divided into four stages, figure 2.16.

The first one is the preoperative stage. In this, the doctor uses the MRI and CT images to determine the target points and to plan the best trajectory. This stage remains unchanged in the proposed procedure.

Secondly, there is the image-to-patient registration. Here several differences are proposed. The proposed method falls into the surface registration category. However, by employing the intraoperative ultrasound technology, it overcomes the problem of the skin mobility. Moreover, the ultrasound transducer will be attached to the robot flange and the robot will be manually guided during the scanning. Thereby, in this stage the robot will be used as a tracker, so that the position of the transducer is known in every instant.

Once the registration is accomplished, the target point and the desired trajectory are transformed to the physical space coordinates and uploaded to the robot controller. The surgeon will exchange the robot tool and guide it to the desired position. In this stage, however, the robot will operate in an impedance control mode, actively correcting the surgeon's action. Besides this, the surgeon can still receive feedback from a screen, where the movement of the tool relative to the patient can be followed in the image space.

Finally, once the robot is correctly positioned, it will constrain every degree of freedom forcing the needle to move only in depth along the desired trajectory, similarly to what was done with the articulating arm.

It is relevant to refer that the use of the aforementioned technologies and procedures comes up as a way to perform the neurosurgical procedure in a more accurate, easy and safe manner. To end with, the work developed in this thesis focuses in evaluating the system's performance in the second and third stages execution.

Chapter 3

Materials and Methodology

3.1 Tracking

3.1.1 KUKA LBR Med

The LBR Med is classified as a lightweight robot and is a jointed-arm robot with 7 axes. The robot is eqquiped with a set of sensors that provide information for the robot control and that are also used for the protective functions. Therefore, every axis contains a range sensor, a torque sensor and a temperature sensor. It is important to refer that the employment of a torque sensor in each joint allows the implementation of a compliant robot behavior, enabling the LBR Med to react very quickly to external forces and makes it particularly suitable for interaction with humans.

Sunrise Workbench

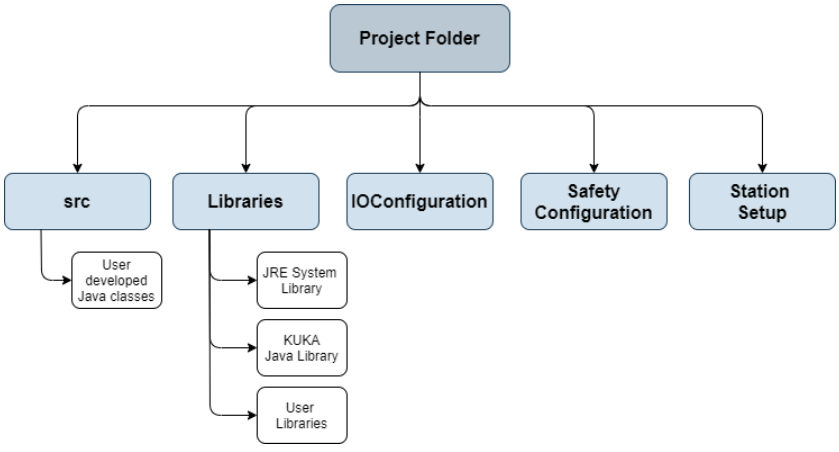

Figure 3.1: Sunrise Workbench Project Organization.

The Sunrise OS is the operative system designed by KUKA to interact with the robot. The robot can be programmed through the Sunrise Workbench application using the Java language.

A regular project in Sunrise Workbench is organized as figure 3.1 shows.

Where:

- **src**: The source code folder that contains every java class developed by the user to perform the project specific tasks.
- **Libraries**: The libraries folder contains both the Java Runtime Environment (JRE) library which allows the developer to interact with the hardware components, the KUKA Java library which contains the Java classes to manipulate the robot, and the user libraries which provide functionality to each specific project.
- **IOConfiguration**: The IOConfiguration allows the developer to interact with external devices through a set of input and output signals provided by the robot controller itself.
- **Safety Configuration**: The Safety Configuration makes possible to use the safety capabilities implemented in LBR Med.
- **Station Setup**: The Station Setup is a configuration file that defines the robot and the controller used in the project.

Path Planning and Robot Control

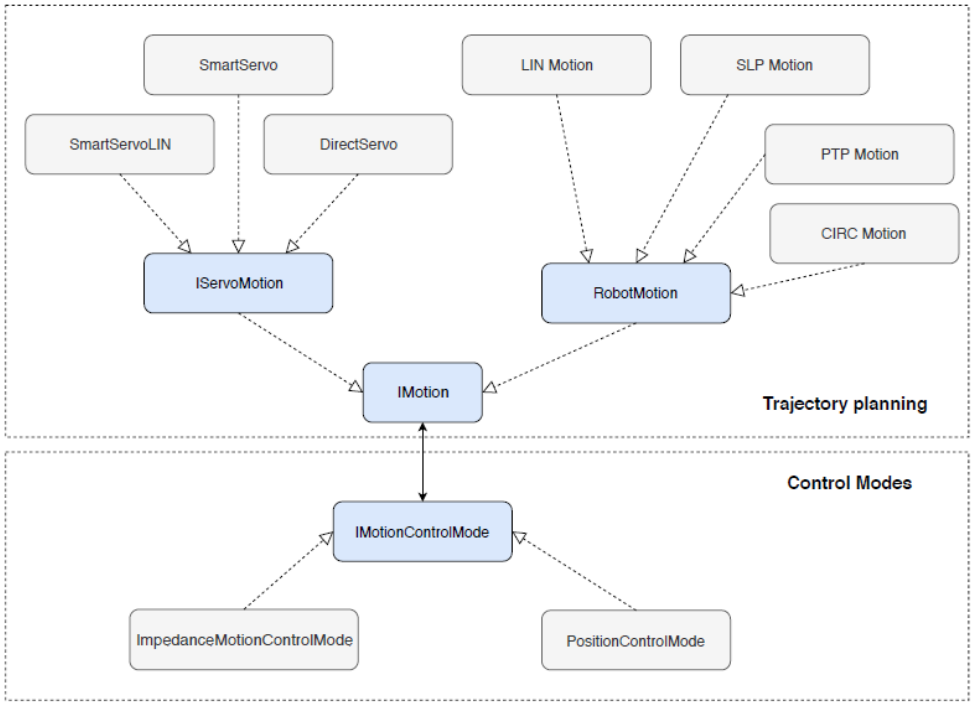

Figure 3.2: Motion and Control Laws. (From [34])

Figure 3.2 shows the robot trajectories and control modes available to command the robot.

On one hand, the *RobotMotion* interface defines the trajectories typically used in industrial robots, such as, linear motion (LIN), point to point motion (PTP), spline motion (SLP) and circular motion (CIRC). These allow the user to define positions, velocities, accelerations and jerk profiles.

The *IServoMotion* interface on the other hand allows the user to change between motions in real time, correcting its trajectories based on external perturbations. However, this will not be used in the

context of this work.

Also, there is the control modes available in *IMotionControlMode*. This interface is implemented by the *ImpedanceMotionControlMode* and the *PositionControlMode*. When using the impedance control mode, the robot reacts compliantly to the external forces applied based on the set impedance parameters. On the other hand, in position control mode, the robot sets each joint stiffness to its maximum and follows the trajectory as close as possible. A detailed description of these control modes is out of the scope of this project.

Finally, it is important to mention that a control mode was programmed which is a particular case of the impedance control mode. This will be called the manual guidance and it is an impedance control mode with zero stiffness.

Communication

Finally, besides positioning the tools, the robot must communicate with the external devices, sending its position and orientation.

The OpenIGTLink comunication protocol was implemented in Java, [4] and a brief description of this communication protocol can be found in section 3.3.1.

3.1.2 Polaris Spectra

The robot as a tracking device has the limitation of only being able to track one object at a time. This is not be a significant problem to perform the surgical procedure, however, to perform the lab experiments, section 3.5, one will need to track more than one object at the same time. Therefore, the Polaris Spectra will be used to perform the calibration steps, to perform several measurements used in the accuracy evaluation and to validate the robot positioning.

The Polaris Spectra, henceforth designated by Polaris, is an optical system developed by Northern Digital (NDI). It can be seen in figure 3.3.

Figure 3.3: NDI Polaris Spectra.

The two cameras placed in the Polaris structure, are infrared light emitters which make possible to locate any reflector in a given working volume. The NDI system provides several tools that can be tracked, which are shown in figures 3.4 and 3.5.

The system uses the relative position between the tool markers to identify the tool and subsequently determines its position and orientation. Thus, the system can track several tools at the same time as long as their geometries are known and different from each other. The tools like the one in figure 3.4 will be used to track important objects and will be called trackers from here on.

Figure 3.4: Polaris Tool.

Figure 3.5: Polaris Stylus.

Also, there is the stylus, figure 3.5. The position of its tip can be easily determined through pivoting, section 3.5.5, and the stylus can be used to measure the position of static points or surfaces in space.

Finally, Wiles et al. [35] evaluated the Polaris Spectra system and reports a mean position error of 0.185 mm and a mean orientation error of 0.383º when tracking a passive rigid body.

3.2 Imaging

3.2.1 CT Scanner

The CT scanner used in this work was the Phillips Brilliance R 64. The scanned image is a volume of 197 slices spaced by 1 mm. Furthermore, each slice has a field of view of 280 mm and consists in a matrix of 512×512 voxels. Therefore, size of each voxel, $[{}^{CT}s_x, {}^{CT}s_y, {}^{CT}s_z]$, is:

$$ {}^{CT}s_x \;=\; {}^{CT}s_y \;=\; \frac{280}{512} = 0.5469\ mm/vx \tag{3.1} $$

$$ {}^{CT}s_z \;=\; 1\ mm/vx \tag{3.2} $$

3.2.2 Aloka ProSound

The device used to acquire ultrasound images was the ProSound 2, shown in figure 3.6, and the linear transducer UST-586-5, shown in fiugre 3.7, both developed by Hitachi Aloka. These acquire b-mode ultrasound images, within a frequency range of 3.75 to 7.5 MHz and a scanning width of 72mm. Several other parameters are configurable in the ProSound 2 such as the acoustic power, the B-gain and the image depth. Setting these parameters correctly was a concern during this work and the way they were set is explained with more detail in sections 4.1.2 and 4.2.3, where the ultrasound imaging is approached.

To establish the communication between the ultrasound device and the main workstation the frame grabber DFG/USB2propcb, which can be seen in figure 3.8, was chosen. This is one of the preconfigured frame grabbers in the PLUS Library, section 3.3.2, and has a maximum frame rate of 25 frames per second with a maximum resolution of 768×576 pixels.

Figure 3.6: Aloka ProSound 2.

Figure 3.7: Aloka UST-586-5.

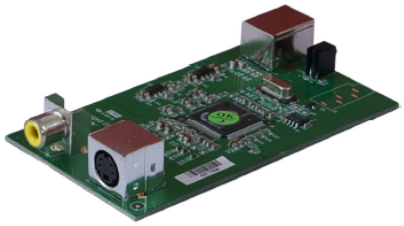

Figure 3.8: Frame Grabber.

3.3 Tracking and Imaging Fusion

3.3.1 OpenIGTLink

The OpentIGTLink protocol was developed by Tokuda et al. [36], and it is an open-source network communication protocol specifically designed for image-guided interventions.

A standard OpenIGTLink message is composed by and header of 58 bytes and the message body of variable length. The header is, in turn, divided into 6 sections: the **version** of the protocol used, the **type** of the message, the **device name**, the device's **time stamp**, the message **body size** and a cyclic redundancy check, **CRC64**.

On the other hand, the message body is specific for each message type. The most important message types in the context of this work were the **transform** messages and the **image** messages. The protocol also allows to communicate the device **status** and **capability** and, by means of a **query mechanism**, allows each device to request or command the stop of a given message sending.

3.3.2 PLUS Toolkit

The Public Software Library for Ultrasound, PLUS toolkit, is an open source project designed by Lasso et al. [37] to integrate the components needed in an image-guided intervention. These can be imaging devices, tracking devices, data processing algorithms and visualization software. An example of the pipeline used by the PLUS toolkit is shown in figure 3.9.

The PLUS toolkit was chosen since it is prepared to work with the devices available, such as the Polaris and the frame grabber. In its turn, the robot was configured as an OpenIGTLink compatible device [37]. PLUS also provides a library with several important applications.

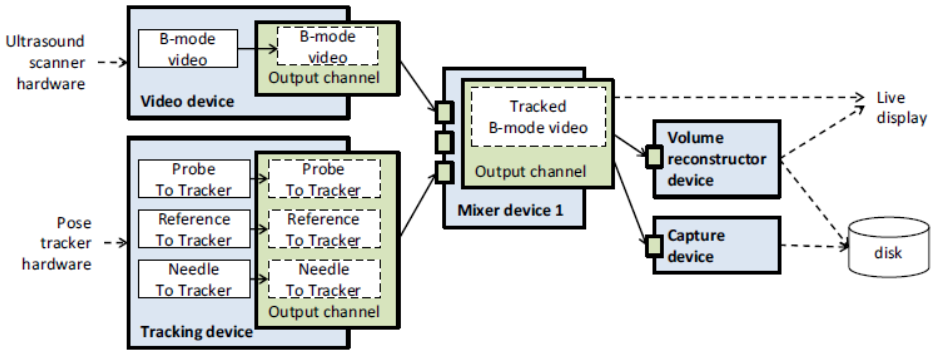

Figure 3.9: PLUS Pipeline Example. (From [37])

The first one is the *Virtual Mixer*. When using different devices, data will be acquired in different time stamps and for that reason it has to be resampled so that it can be combined together in a coherent sampling time. The data fusion is performed by the *Virtual Mixer*. Furthermore, to successfully combine the data, all the devices must be synchronized in time, so that every device's time stamp correspond. This is accomplished through temporal calibration, which is explained in detail in section 4.2.1, and is also performed by another PLUS application.

The *Capture Device*, was used to save the output of the *Virtual Mixer* throughout the experiments and generate a MHA file with the interesting data, so it could be easily used in Matlab.

PLUS also provides a live streaming output through an OpenIGTLink connection. The 3D Slicer, section 3.3.3, was used as a visualization tool, connected to the PLUS output stream.

Finally, PLUS offers a ultrasound imaging simulator, Bartha et al. [38], which can be used as a PLUS device and that was used to make preliminary tests to the registration algorithms. This simulator computes the scanlines using a simple physics model which includes attenuation, absorption, surface reflection and speckle.

3.3.3 3D Slicer

The 3D Slicer, originally developed by Pieper, Halle, and Hikinis [39], is an open-source software platform for medical imaging processing and visualization.

This software is composed by a group of modules which can perform specific tasks like filtering, segmenting, applying transformations or even choosing visualization parameters. It also allows the user to program new modules to join functionalities and automate processes.

A specific set of modules in 3D Slicer, which comes in *SlicerIGT* package, are the ones that allow it to command and communicate with a PLUS server through an OpenIGTLink connection.

Although the said wide range of applications, programming new modules is not easy due to the poor documentation available, and the use of each module in separate does not allow user-developed algorithms to be implemented. For that reason, in this work, the 3D Slicer will be used merely to command the PLUS and to visualize the data during the experiments. It will also be used to visualize the CT images and, sporadically, whenever there is no need to automate a task, one will take advantage of 3D

Slicer capabilities.

3.3.4 Setup

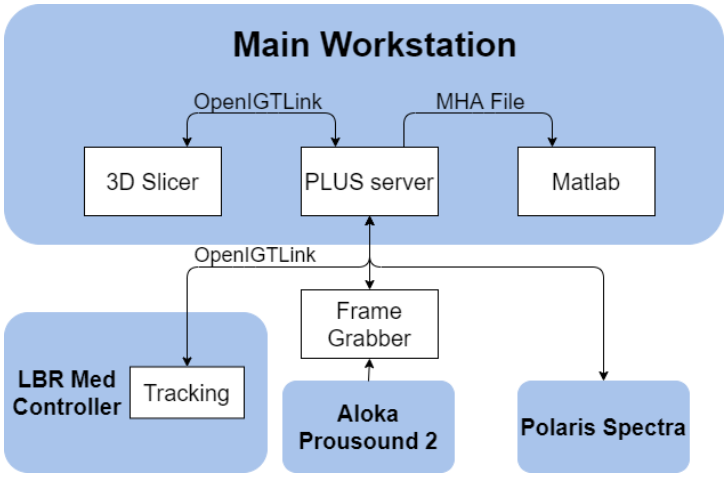

Figure 3.10: Devices setup.

Figure 3.10 shows how every piece of software and hardware described throughout this section is combined together in an experiment. As a summary of what have been explained, important data comes from the robot and the Polaris which are used as trackers to measure poses in space, and from the Ultrasound which sends images through the frame grabber. A PLUS server is used to synchronize all this information and the 3D Slicer is used to command the PLUS and visualize the data. Finally, PLUS saves the important data in a MHA file which is then used by the Matlab where the self-developed algorithms will run. The main workstation used in this work is a computer with an Intel i5-5200U processor running at 2.20 MHz using 6 GB of RAM.

3.4 Phantom

The main study object in this work is an anthropomorphic phantom based on the human cranium. It was designed using a CAD software and built using the three-dimensional (3D) printer *Stratasys Dimension R* in acrylonitrile butadiene styrene (ABS). The advantage of using this material is both that it makes the 3D printing easy while it is also easily detected in both US and CT image modalities.

Its dimensions are very similar to the average human cranium: 305 mm height, 178 mm width and 203 mm length. Figures in 3.11 show the front and side views of the phantom, respectively.

Inside the phantom, a group of spheres were placed. These will be used as targets, simulating points and trajectories. Figures in 3.12 show these spheres geometry.

Figure 3.12b also shows what will be referred to as the target position and orientation, p_{Target} and v_{Target}, relative to the target sphere itself.

Finally figure 3.13 shows the top view of the phantom with the targets spheres placed. These are numbered from 1 to 10 and this numbering will be used throughout this document to indicate each target.

(a) (b)

Figure 3.11: Phantom front view in (a). Side view in (b). (From [1])

(a) Sphere geometry. (From [24]) (b) Sphere Cut. (Adapted from [24])

Figure 3.12: Target sphere.

Figure 3.13: Phantom top view with numbered targets. (Adapted from [1])

3.5 Methodology

3.5.1 Reference Frames

To start with, it is important to introduce the principal frames of reference. Figure 3.14 shows the main frames of reference present in physical space. These are the *Polaris*, the robot *Base* and the robot

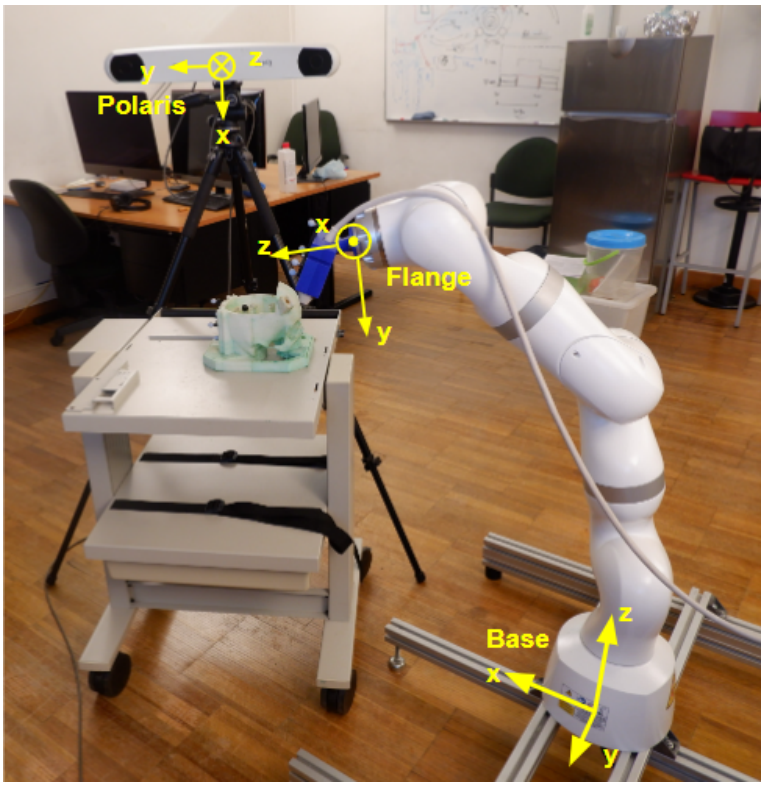

Figure 3.14: Frames of reference in physical space.

Flange reference frames. On the other hand, figure 3.15 shows the frames of reference associated with the Polaris tools.

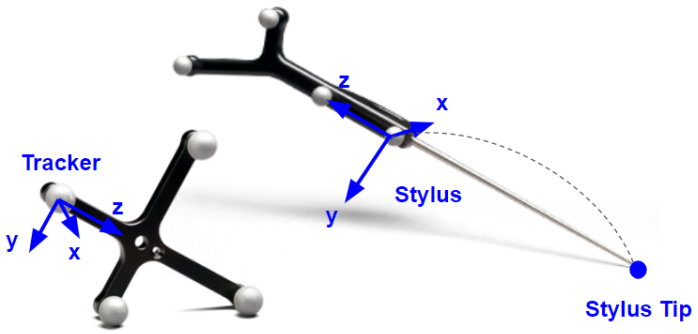

Figure 3.15: Polaris tools reference frames.

Regarding the images frames of reference, figures in 3.17 show the frame of reference of the CT image space while figure 3.16 show the frame of reference of the ultrasound image.

Finally, there is also the needle reference frame which is shown ahead in this section in figure 3.22.

3.5.2 Targets

The targets, figure 3.13, play an important role since it is through them, that the errors will be calculated. The position and orientation of the targets in the CT space, p^{CT}_{Target} and v^{CT}_{Target}, were determined manually using the 3D Slicer segmentation capabilities. Two points were segmented in Slicer: the bot-

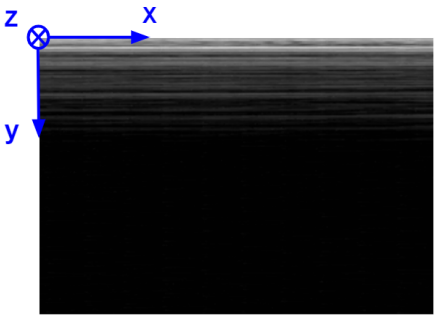

Figure 3.16: Ultrasound image reference frame.

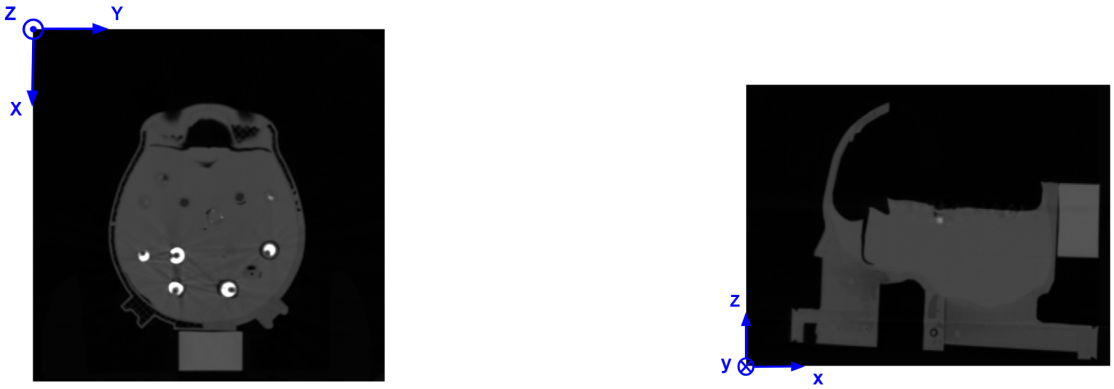

(a) Axial Plane

(b) Sagittal Plane

Figure 3.17: CT reference frame.

tom of the sphere and a point along the sphere hole. These can be seen in figure 3.18,

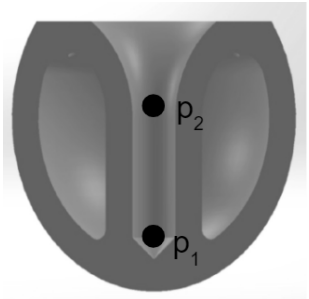

Figure 3.18: Points segmented in Slicer. (Adapted from [24])

The position and orientation of the target were then calculated through 3.3 and 3.4.

$$p_{Target}^{CT} = p_1 \tag{3.3}$$

$$v_{Target}^{CT} = \frac{p_2 - p_1}{\|p_2 - p_1\|} \tag{3.4}$$

On the other hand, the position of each target was determined in the physical space using the stylus. The stylus tip was inserted inside each target sphere, as shown in figure 3.19, and its position with reference to the base of the robot was calculated, equation 3.5.

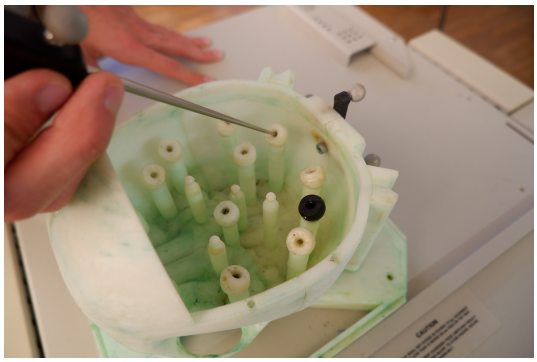

Figure 3.19: Targets position acquisition

$$p_{Target}^{Base} = T_{Polaris}^{Base} \cdot T_{Stylus}^{Polaris} \cdot p_{Tip}^{Stylus} \tag{3.5}$$

The orientations in physical space were estimated through the orientations measured in the CT scan. A ground truth transformation between the CT and the base reference frames, $T_{CT}^{\prime Base}$, was determined by registering the targets, equation 3.6, and the orientation of each target with reference to the base was calculated by applying the aforementioned transformation to each orientation in CT scan, equation 3.7.

$$\sum_{i} \left\| p_{Target,i}^{Base} - T_{CT}^{\prime Base} \cdot p_{Target,i}^{CT} \right\| \tag{3.6}$$

$$v_{Target}^{Base} = T_{CT}^{\prime Base} \cdot v_{Target}^{CT} \tag{3.7}$$

3.5.3 Registration

It was stated that, in the context of this work, the registration is the process of estimating the coordinate transformation between the image space and the physical space. Since the robot is the only tracking device intended to be used in the surgical room, the aforementioned transformation is the transformation between the CT and the robot base reference frames.

Point Clouds

There are three important point clouds to perform the registration experiment in the laboratory.

The first important point cloud is the one that results from the CT image segmentation. The CT segmentation was performed in Matlab and the result was the set of points $p_{Phantom}^{CT}$ defining the phantom surface relative to the CT reference frame.

The second is the one that results from the ultrasound scanning. The surface of the phantom was imaged using the ultrasound probe, as shown in figure 3.20. This was attached to the flange of the robot which was controlled in manual guidance during the process. An algorithm was developed in Matlab to segment the phantom surface in each ultrasound image. The position of each segmented pixel relative to the ultrasound reference frame, $p_{Phantom}^{Ultrasound}$, was determined and subsequently transformed to the

base reference frame, equation 3.8.

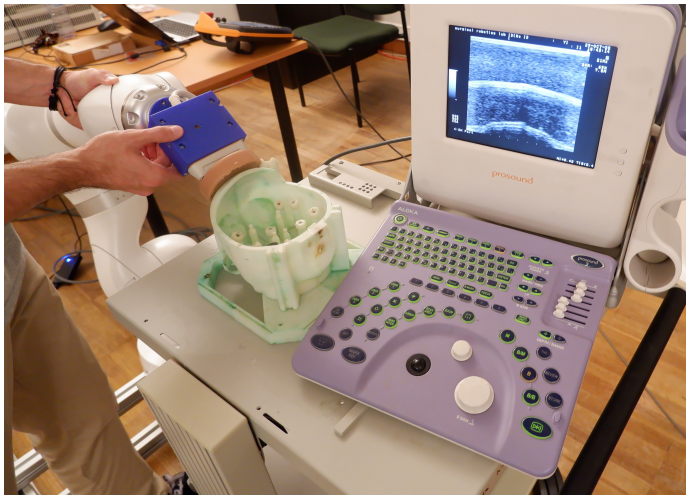

Figure 3.20: Ultrasound point cloud acquisition.

$$p^{Base}_{Phantom} = T^{Base}_{Flange} \cdot T^{Flange}_{Ultrasound} \cdot p^{Ultrasound}_{Phantom} \tag{3.8}$$

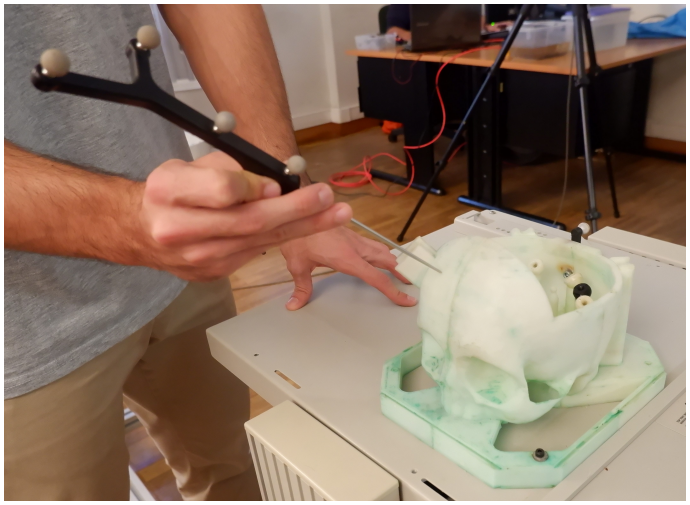

Figure 3.21: Ground truth point cloud acquisition.

Finally, there is the ground truth point cloud. This point cloud was acquired with the Polaris stylus, by sliding its tip over the phantom surface, as shown in figure 3.21, and then transformed to the base reference frame, equation 3.9. It will be used, as common reference, to perform a stepwise evaluation of the error.

$$p^{Base}_{Phantom} = T^{Base}_{Polaris} \cdot T^{Polaris}_{Stylus} \cdot p^{Stylus}_{Tip} \tag{3.9}$$

Notice that both the point cloud acquired with the ultrasound and with the stylus are defined by the set of points $p^{Base}_{Phantom}$, this means that these point clouds should define coincident surfaces. However, due to several sources of inaccuracy, the two point clouds will not overlap perfectly. For that reason and to distinguish these, through the remaining of this section, one will assume that the point cloud acquired

by the ultrasound exists in a virtual reference frame, $Base'$, and thus is defined by the points $p_{Phantom}^{Base'}$.

Stepwise Error Evaluation

In order to assess how each source of inaccuracy affects the final result, the registration will be performed in three steps. For each of those, there was calculated the target position errors, e_p, and the target orientation errors, e_v, to assess the registration quality.

1. The first step consists in registering the CT and the ground truth point clouds. The transformation matrix that results from this step is the T_{CT}^{Base} and the error will be evaluated with equations 3.10 and 3.11.

$$e_p = \left\| p_{Target}^{Base} - T_{CT}^{Base} \cdot p_{Target}^{CT} \right\| \tag{3.10}$$

$$e_v = cos^{-1}\left(v_{Target}^{Base} \cdot (T_{CT}^{Base} \cdot v_{Target}^{CT}) \right) \tag{3.11}$$

2. The second step consists in registering the ultrasound and the ground truth point clouds. If the aforementioned sources of inaccuracy did not exist, the result of this registration would be the identity matrix. However, as mentioned previously, this is not what happens in reality and thus, a transformation matrix, $T_{Base}^{Base'}$, different from the identity results from this registration. The error for this step will be evaluated through equations 3.12 and 3.13.

$$e_p = \left\| p_{Target}^{Base} - T_{Base}^{Base'} \cdot p_{Target}^{Base} \right\| \tag{3.12}$$

$$e_v = cos^{-1}\left(v_{Target}^{Base} \cdot (T_{Base}^{Base'} \cdot v_{Target}^{Base}) \right) \tag{3.13}$$

3. Finally, the main step is to register the CT and the ultrasound point clouds. This will be evaluated using the equations 3.14 and 3.15, where $T_{CT}^{Base'}$ is the transformation that resulted from this step.

$$e_p = \left\| p_{Target}^{Base} - T_{CT}^{Base'} \cdot p_{Target}^{CT} \right\| \tag{3.14}$$

$$e_v = cos^{-1}\left(v_{Target}^{Base} \cdot (T_{CT}^{Base'} \cdot v_{Target}^{CT}) \right) \tag{3.15}$$

Accuracy Determination

Since the registration quality is very sensitive to the ultrasound images acquisition, every step that requires this acquisition was performed N times, using independent scans. The mean and the standard deviation were calculated for each target error using equations 3.16 and 3.17, where the letter e is representing both position and orientation errors.

$$\mu_e = \frac{1}{N}\sum_{i=1}^{N} e_i \tag{3.16}$$

$$\sigma_e = \frac{1}{N}\sum_{i=1}^{N} \sqrt{(e_i - \mu_e)^2} \tag{3.17}$$

Finally, the computational time was also computed for each algorithm intended to be used in the surgical procedure, so to conclude whether or not its use is feasible.

3.5.4 Needle Positioning

A needle holder was built as figure 3.22 shows. It is a tool that can be attached to the robot flange and that allows the needle to be pushed through, limiting its movement to a line in space, to simulate the real procedure.

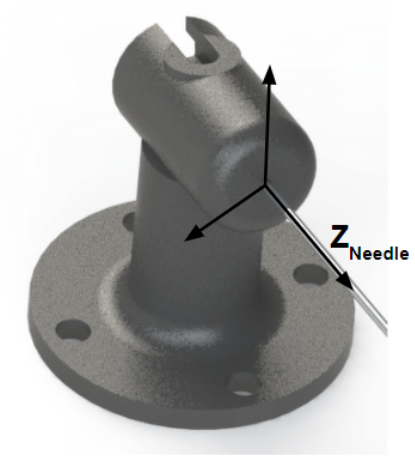

Figure 3.22: Needle holder.

The needle frame of reference, introduced in the beginning of this section, is attached to the holder and it was determined so that the physical needle is along the Z axis. Also, its origin is placed in the center of the hole in the outermost surface of the holder, as it can be seen in the figure.

Having said so, placing the needle means to command the robot to align the Z axis of the needle frame of reference with the target orientation, figure 3.23. Since it is the doctor's job to push the needle forward through its path until it reaches the target, a distance, d, must be kept between the origin of the needle reference frame and the target position, p^{Base}_{Target}. Figure 3.24 shows the robot positioning the needle in the laboratory.

Finally, this can be summed up to compute the matrix T^{Base}_{Flange} that holds equations 3.18 and 3.19.

$$p^{Base}_{Target} = T^{Base}_{Flange} \cdot T^{Flange}_{Needle} \cdot \begin{bmatrix} 0 \\ 0 \\ d \\ 1 \end{bmatrix} \tag{3.18}$$

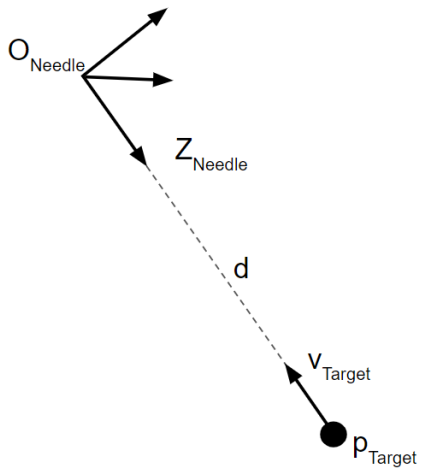

Figure 3.23: Reference frames in needle placement.

Figure 3.24: Needle placement in the laboratory.

$$v_{Target}^{Base} = T_{Flange}^{Base} \cdot T_{Needle}^{Flange} \cdot \begin{bmatrix} 0 \\ 0 \\ -1 \\ 0 \end{bmatrix} \tag{3.19}$$

Stepwise Error Evaluation

Just like in the previous section, the error evaluation was performed in two steps:

1. In the first step, the robot was commanded to the positions acquired by the stylus, in this, no information from the CT space will be used. In this step the left side of equations 3.18 and 3.19 is given by 3.5 and 3.7, respectively.

2. In the second step, the robot was be commanded to the positions estimated through the registration between CT and ultrasound point clouds. In this step p_{Target}^{Base} and v_{Target}^{Base}, of equations 3.18 and 3.19, are substituted by $p_{Target}^{Base'}$ and $v_{Target}^{Base'}$ and are given by:

$$p_{Target}^{Base'} = T_{CT}^{Base'} \cdot p_{Target}^{CT} \tag{3.20}$$

$$v_{Target}^{Base'} = T_{CT}^{Base'} \cdot v_{Target}^{CT} \tag{3.21}$$

It is important to refer that throughout these experiments, the robot was commanded using the point to point (PTP) instructions, different than what happens in a real surgical environment where the robot is guided by the doctor in an impedance control regime.

Finally, a tracker was attached to the needle holder and the error was calculated in the Polaris reference frame for both the described steps. It was then evaluated through the equations 3.22 and 3.23.

$$e_p = \left\| p_{Target}^{Polaris} - T_{Tracker}^{Polaris} \cdot T_{Needle}^{Tracker} \cdot \begin{bmatrix} 0 \\ 0 \\ d \\ 1 \end{bmatrix} \right\| \tag{3.22}$$

$$e_v = cos^{-1} \left(v_{Target}^{Polaris} \cdot \left(T_{Tracker}^{Polaris} \cdot T_{Needle}^{Tracker} \cdot \begin{bmatrix} 0 \\ 0 \\ -1 \\ 0 \end{bmatrix} \right) \right) \tag{3.23}$$

3.5.5 Calibrations

Up to now, several transformation matrices were mentioned. Some of those are given while others must be calculated through calibration.

Tip to Stylus

To start with, there is the position of the stylus tip relative to the stylus reference frame. This is calculated through pivoting, which consists in rotating the stylus around the tip, describing a conic shape. Also, the tip position must be kept still throughout the procedure. Then, the NDI software computes automatically the stylus tip position. The estimation is accomplished by optimizing the cost function in equation 3.24, where p_0 is the fixed position of the stylus tip.

$$\sum_i \left\| p_0 - T_{Stylus,i}^{Polaris} \cdot p_{Tip}^{Stylus} \right\| \tag{3.24}$$

Ultrasound to Flange

The transformation between the ultrasound frame of reference and the flange of the robot. This is the transformation that allows the ultrasound image to be positioned in space. A huge effort was put into accurately determine this transformation since correctly positioning the images has an enormous impact in ultrasound volume reconstruction and registration. The method used was the calibration with a stylus, [40]. However, some improvements were made so to make it automatic and more accurate. The method is explained in detail in section 4.2.3. Following the recommendations on [40] the calibration procedure was performed N times and its quality assessment was made by evaluating its accuracy and precision.

The accuracy was calculated through the Point Reconstruction Accuracy, PRA. This is in turn computed by imaging a group of J points, of which the positions are known. The known positions are then compared with the estimated ones through equation 3.25.

$$PRA = \frac{1}{N}\sum_{i=1}^{N}\left(\frac{1}{J}\sum_{j=1}^{J}\left\|p_j^{Base} - T_{Flange}^{Base}\, T_{Ultrasound,i}^{Flange}\, p_j^{Ultrasound}\right\|\right) \tag{3.25}$$

On the other hand, the precision is calculated through the Calibration Reproducibility, CR. This is obtained by transforming several pixels in the image with the estimated transformations and computing how near they are across the N trials. The standard way to do it is by using the four corners and the center of the image. Equation 3.26 shows how CR is calculated for each point.

$$CR = \frac{1}{N}\sum_{i=1}^{N}\left\|\overline{p}^{Flange} - T_{Ultrasound,i}^{Flange}\, p^{Ultrasound}\right\| \tag{3.26}$$

Where $\overline{p}^{Flange}$ is calculated with equation 3.27. The results for this calibration can be seen in section 5.1.

$$\overline{p}^{Flange} = \frac{1}{N}\sum_{i=1}^{N} T_{Ultrasound,i}^{Flange}\, p^{Ultrasound} \tag{3.27}$$

Polaris to Robot Base

The transformation between the robot base and the Polaris reference frame. This transformation is needed to perform every experiment that uses both the robot and the Polaris. To compute this transformation matrix the robot was commanded to several different positions while its flange was tracked by the Polaris. The transformation was estimated through a point-pair registration. A detailed description of the procedure can be found in section 4.2.2.

Needle to Flange/Tracker

Finally, the transformation between the needle frame of reference and the flange or tracker frames of reference. This transformations are responsible for allowing the robot to correctly place the needle in space while the Polaris measurements can be used to compute the placement error. A simple method was developed to accomplish this calibration and it is described in detail in section 4.2.4.

Chapter 4

Implementation and Algorithms

4.1 Segmentation

In this section, every image processing techniques used to segment the CT and ultrasound images will be described. It is important to mention that segmenting these images means to extract a point cloud that defines the phantom outer surface. To achieve this, firstly the pixels/voxels that define this surface must be found and secondly, the position of these must be determined in the desired reference frame.

4.1.1 CT Segmentation

Starting with the CT volume, this has the characteristics shown in section 3.2.1. Also, figures 4.1a to 4.1c show three particular slices of the phantom CT volume in the axial, coronal and sagittal planes. The CT segmentation was performed applying 2D image processing techniques to each individual axial slice.

(a) Axial Plane (b) Coronal Plane (c) Sagittal Plane

Figure 4.1: Phantom CT Planes.

The phantom is defined by the voxels with the higher intensities and thus the first step was the application of a threshold. Figures in 4.2 show the result of this procedure. To favour the visualization, the binary images shown in this report will have their foreground and background colours inverted, i.e., the background will be represented by the white pixels and the foreground will be represented by the

black pixels.

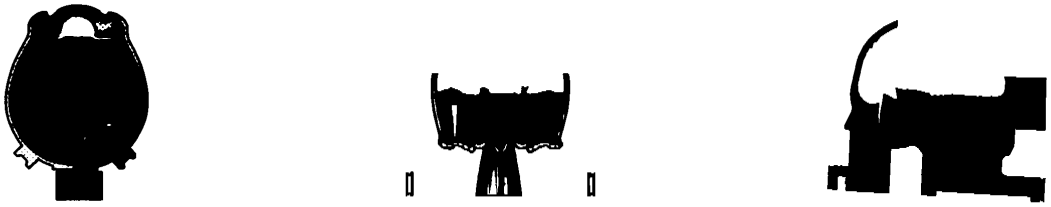

(a) Axial Plane (b) Coronal Plane (c) Sagittal Plane

Figure 4.2: Threshold application result.

The next step was to find the voxels which define the phantom contour. A searching strategy was implemented to keep only the black voxels which define the border of the phantom in each axial slice. For each slice the rows and columns were searched, and, in each row and column, both directions were covered, i.e., right to left and left to right for rows, and top to bottom and bottom to top for columns, adding up to a total of four loops. Having said so, the first black voxel found in each line or column in each direction was considered to be part of the outer surface. Figures in 4.3 show the output of this procedure, while figure 4.4 show the axial slice where the segmented surface overlaps the original image.

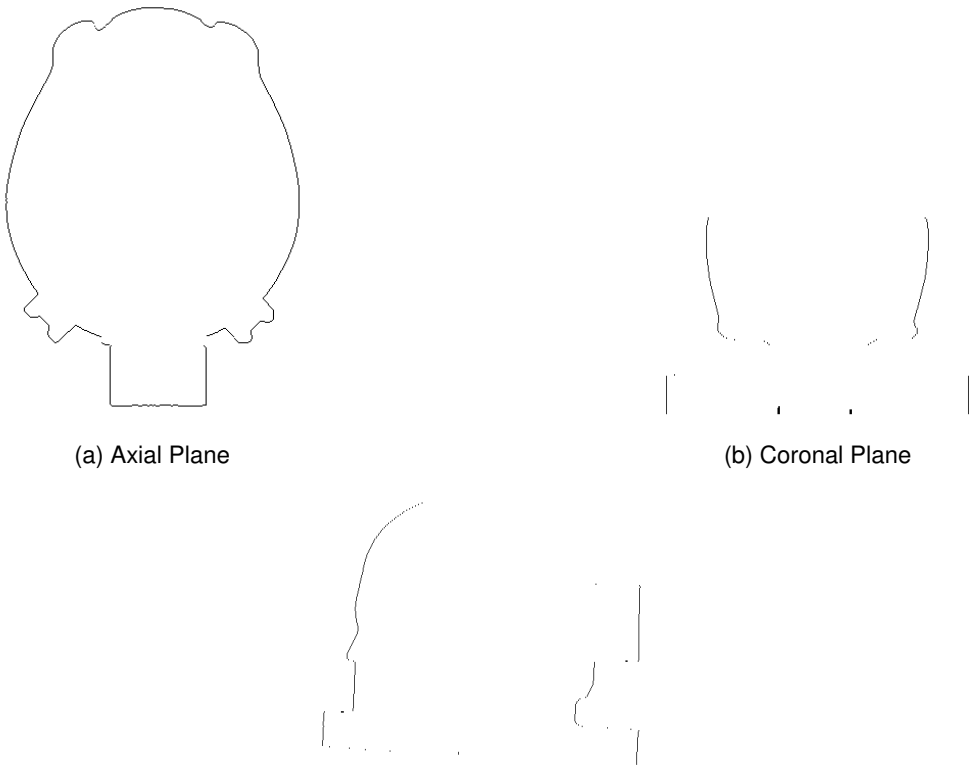

(a) Axial Plane (b) Coronal Plane

(c) Sagittal Plane

Figure 4.3: Surface extraction result.

The position of each segmented voxel was then computed relative to the CT reference frame, by

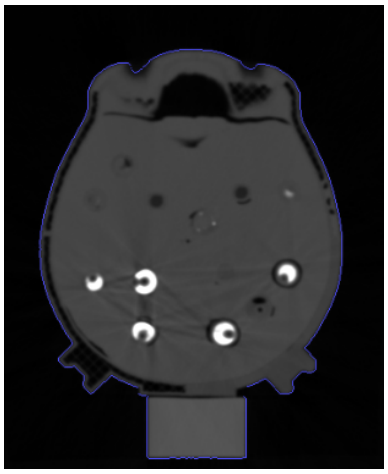

Figure 4.4: Segmented surface and original image overlapped.

converting it to millimeters, as shown in equation 4.1.

$$p^{CT}_{Phantom} = \begin{bmatrix} {}^{CT}s_x & 0 & 0 & 0 \\ 0 & {}^{CT}s_y & 0 & 0 \\ 0 & 0 & {}^{CT}s_z & 0 \\ 0 & 0 & 0 & 1 \end{bmatrix} \cdot \begin{bmatrix} {}^{CT}vx_i \\ {}^{CT}vx_j \\ {}^{CT}vx_k \\ 1 \end{bmatrix} \tag{4.1}$$

After applying this procedure, the resulting point cloud was too dense, which caused every operation on the point cloud to take too long to process. For that reason a downsampling step was applied. The method used for this step was the grid average. In this a three dimensional grid is defined with a given grid step and the points within the same box are merged to a single point. This is done preserving the point cloud shape. The definition of this grid step was specific for each registration step, however figure 4.5 shows the CT point cloud in which, for visualization purposes, the grid step was set to 3 mm.

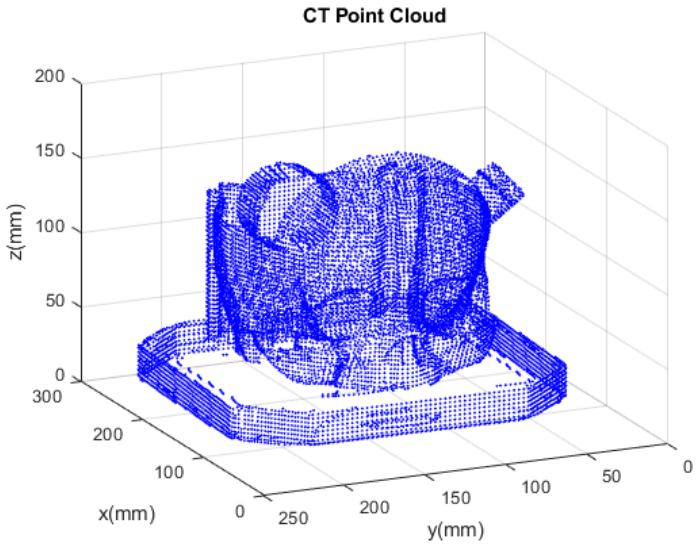

Figure 4.5: Segmented point cloud.

4.1.2 Ultrasound Segmentation

Setup

The first important machine parameter is the image depth. This were set to the minimum allowed by the ProSound, i.e., $\approx 47\ mm$, since the surface of the phantom will always appear in the upper pixels. Also, by choosing the minimum depth, the image resolution will be the highest. The size of each pixel was directly given by the machine and it was:

$$^{US}s_x = ^{US}s_y = 0.1168mm/px \tag{4.2}$$

The images were further clipped to a 200×465 pixels region of interest, as shown in figure 4.6.

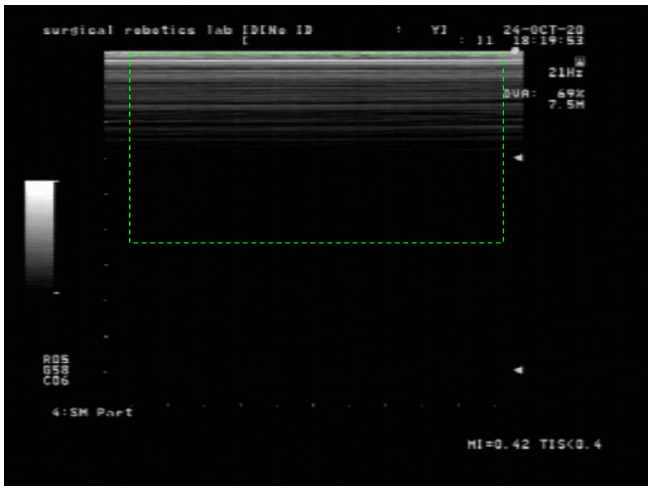

Figure 4.6: Clipped ultrasound frame.

Also, since one is working with the upper part of the image, the frequency was chosen to be the highest, i.e., 7.5 MHz. The acoustic power was set to 60% and the B-gain was set to 55. These were tuned by hand to reduce the image noise with no degradation of the imaged phantom surface.

Image Segmentation

A regular ultrasound image of the phantom surface can be seen in figure 4.7.

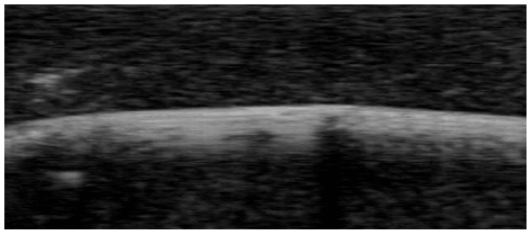

Figure 4.7: Phantom surface ultrasound image.

The first step in the segmentation was to apply a Gaussian filter to smooth the imaged surface. The output can be seen in figure 4.8.

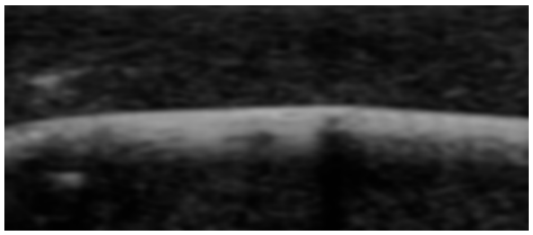

Figure 4.8: Ultrasound image filtered.

After the filtering, a threshold was applied. Like in the previous section, for visualization purposes, the phantom surface (image foreground) is represented by the black pixels while the image background is represented by white pixels. The result of the threshold application can be seen in figure 4.9. In this, it is possible to verify that some artifacts appear as black pixels too due to some unfiltered noise.

Figure 4.9: Ultrasound binary image.

The elimination of these artifacts assures that the resulting point cloud will not contain outliers. The solution was to determine the connected components in the binary image and keep only the largest one. In its turn, finding the connected components can be divided in three steps:

1. Search for the next unlabeled pixel , ρ, i.e., a segmented pixel that does not belong to any connected component.
2. Determine every segmented pixel that connects to ρ using a flood-fill algorithm.
3. Repeat steps 1 and 2 until there is no more unlabeled pixels.

The result of applying this elimination can be seen in figure 4.10.

Figure 4.10: Clean ultrasound binary image.

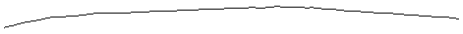

Figure 4.11: Extracted surface.

Finally, the outer surface was extracted by keeping only the highest pixel of every column. The result can be seen in figure 4.11 and in figure 4.12 where the segmented surface overlaps the original image.

The position of each segmented pixel was converted to millimeters as shown in equation 4.3 and finally, their position relative to the robot base reference frame was calculated through equation 3.8.

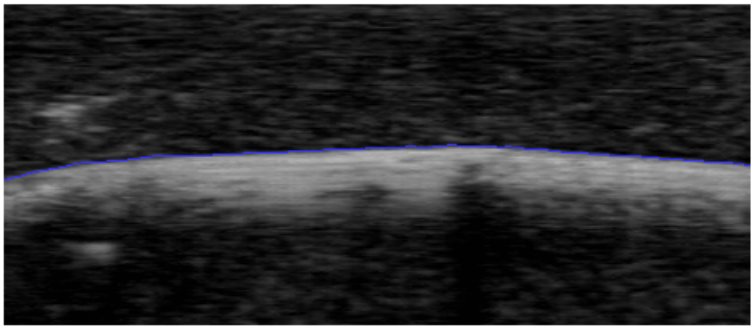

Figure 4.12: Extracted surface and original image overlapped.

$$p_{Phantom}^{Ultrasound} = \begin{bmatrix} {}^{US}s_x & 0 & 0 & 0 \\ 0 & {}^{US}s_y & 0 & 0 \\ 0 & 0 & 0 & 0 \\ 0 & 0 & 0 & 1 \end{bmatrix} \cdot \begin{bmatrix} {}^{US}px_i \\ {}^{US}px_j \\ 0 \\ 1 \end{bmatrix} \tag{4.3}$$

Also, just like in the previous section, the resulting point cloud had to be downsampled. This was performed in the same way as for the CT cloud. Figure 4.13 shows the resulting point cloud of the phantom forehead where, for visualization purposes, the grid step was set to 1 mm.

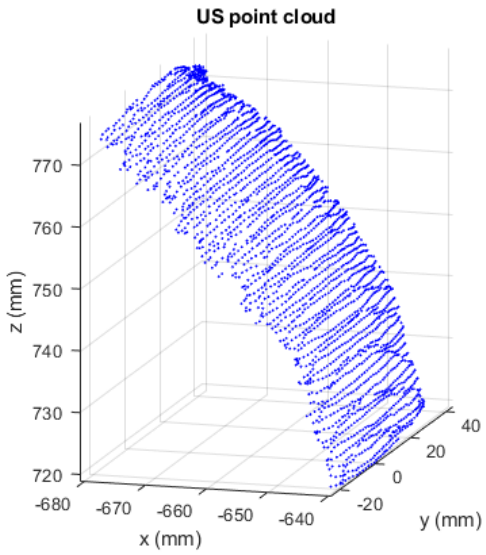

Figure 4.13: Ultrasound point cloud.

4.2 Calibration

4.2.1 Temporal Calibration

It was referred in section 3.3.2, that the data from the different devices is merged by the *Virtual Mixer*. However, the internal time stamp is specific for each device, which may cause a time shift to appear between the messages from different devices. For instance, a position sent from the robot could be associated with the wrong position sent by the Polaris which would result in inconsistent tracking. Such time shift can be corrected in PLUS by applying a delay to each individual device messages.

To compute this delay Moult et al. [41] proposes a temporal calibration method which is embedded in PLUS. The procedure consists in imaging the bottom of a water tank while performing a sinusoidal movement, in the direction perpendicular to the bottom of the tank, with the ultrasound probe. The bottom of the tank is automatically segmented by the PLUS using a RANSAC algorithm, [41], and its position in the images will consequently describe a sine wave as well. Figures in 4.14 show the segmented bottom of the tank.

(a) (b)

Figure 4.14: Segmented bottom of the tank. In (a) the probe was away from the bottom of the tank while in (b) the probe was closer to the bottom of the tank. (Adapted from [41])

Having these signals, i.e., the probe movement and the bottom tank position in the ultrasound image, the time shift can be determined by aligning the two. Figure 4.15 shows the two sine waves before the calibration and 4.16 shows the two sine waves after the calibration. In both, the fixed signal corresponds to the position of the bottom of the tank in the image while the moving signal corresponds to the position of the ultrasound probe, i.e., the tracking signal. The correction is done by shifting the moving signal to match the fixed signal.

Since there was the need to synchronize the messages from three devices, the adopted method was to define the ultrasound time delay to be zero and perform the calibration twice. One calibration was performed with the tracking signal coming from the robot and another with the tracking signal coming from the Polaris. Thus, a time delay was computed for the robot messages and a different one was computed for the Polaris messages.

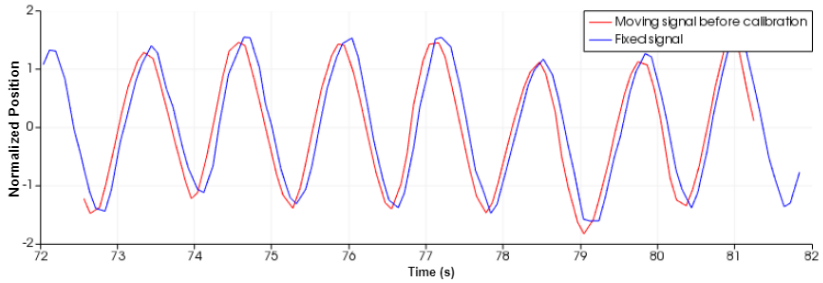

Figure 4.15: Sines before calibration.

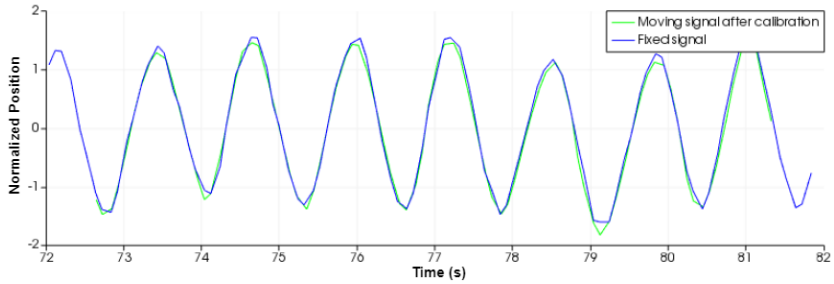

Figure 4.16: Sines after calibration.

4.2.2 Robot-Polaris Calibration

Tovar-Arriaga et al. [42] uses a simple method to calibrate a robot with a navigation system. This method consists in commanding the robot to move its flange, while this is being tracked by the navigation system. Resulting from this procedure, there is the set of flange positions with reference to the robot base, and the set of flange positions with reference to the navigation system. Finally, a least-squares optimization can be used to estimate the coordinate transformation between the base and the navigation system reference frames. Figure 4.17 shows the setup of this calibration.

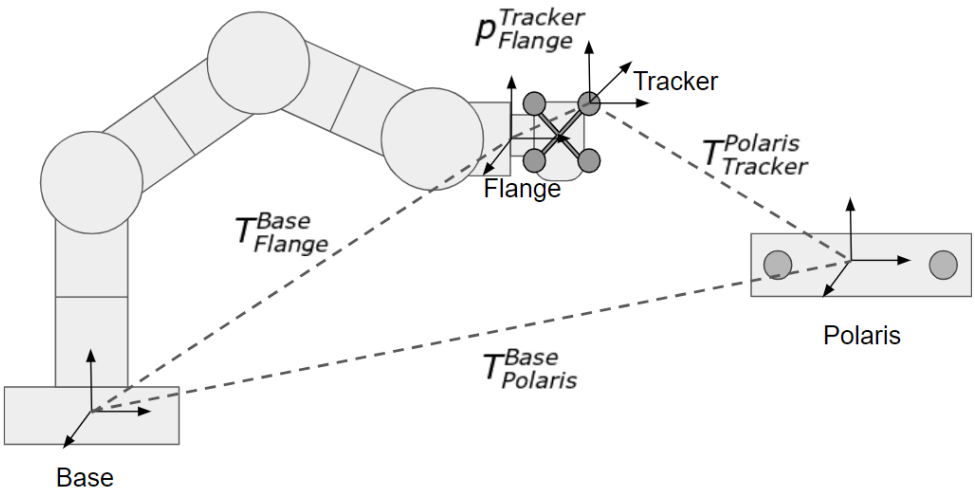

Figure 4.17: Polaris to Base Calibration.

This calibration can be performed in two steps:

1. Determining $p_{Flange}^{Tracker}$ through pivoting. In this step the robot was commanded to keep the flange position still while changing its orientation. The flange orientation was varied from around -70° to +70° in both x, y and z directions, and then the NDI software computed the position of the flange reference frame origin relative to the tracker reference frame.

2. Determining $T_{Polaris}^{Base}$ through a point-pair registration. The robot was commanded to move its flange to 150 different positions. Also, to avoid synchronization errors, at every position the robot stopped for 2 seconds. A Matlab algorithm was developed to record every position read by the robot and by the polaris, and the registration problem was formulated, equation 4.4, and solved through a least-squares minimization.

$$\sum_{i} \left\| T_{Flange,i}^{Base} \cdot \begin{bmatrix} 0 \\ 0 \\ 0 \\ 1 \end{bmatrix} - T_{Polaris}^{Base} \cdot T_{Tracker,i}^{Polaris} \cdot p_{Flange}^{Tracker} \right\| \tag{4.4}$$

4.2.3 Ultrasound Spatial Calibration

The ultrasound spatial calibration is the process of estimating the coordinate transformation between the ultrasound image and the probe position sensor. In the case of this work this is the transformation between the ultrasound and the flange reference frames.

Several methods were studied and attempted to perform the ultrasound spatial calibration. The wall phantom calibration method, [40], was initially chosen due to its simplicity, however, the tests performed shown poor accuracy, and thus, one had no other option but to abandon this method. The most logical option to choose next would be the Cambridge phantom. This was proposed by Prager et al. [43] so to increase the wall phantom accuracy by solving its drawbacks. However, the apparatus and the complex scanning pattern required, [43], made this method unpractical to perform with the robot. Finally, one realized that keeping the probe and the robot still was the most effortless way to perform the calibration. The stylus method was chosen based on this condition and on the material available.

In the traditional method, the stylus is manually aligned with the image, the image is captured and the stylus tip is manually segmented. The procedure is repeated several times changing the image region where the stylus tip appear so to constrain the largest image area possible. The transformation between the image and the probe sensor is estimated through a least squares minimization of 4.5, where $p_{Tip}^{Ultrasound}$ corresponds to each segmented pixel and $T_{Ultrasound}^{Sensor}$ is the estimated transformation. Improvements to this procedure were done, for example, by automatically segmenting the images, [44].

$$\sum_{i=1}^{N} \left\| p_{Tip,i}^{Sensor} - T_{Ultrasound}^{Sensor} p_{Tip,i}^{Ultrasound} \right\| \tag{4.5}$$

Hsu et al. [44] reviews the existing calibration techniques that use a stylus and reports a high precision and good accuracy. Also, he finds the misalignment between the image and the stylus, the most significant source of error.

In this work, one attempted to reduce the error introduced by the aforementioned misalignment so to increase the accuracy of the method. The idea behind the attempted solution is to keep the probe still and slowly move the stylus in the direction perpendicular to the scan plane while keeping it parallel to this plane, as figure 4.18 shows.

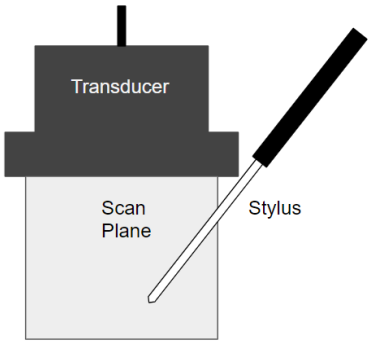

Figure 4.18: Stylus parallel to the scan plane.

By moving the stylus in and out of the scan plane it is possible to assure that at some point it will be perfectly aligned with the plane. It is, then, needed to find a criteria to choose the frame that captured the best alignment.

Figure 4.19 shows, in a simplified manner, what happens when the stylus is moved the described way. Also, in this figure, the blue arrow represents the ultrasound wave emitted by the probe and the red arrow represents the ultrasound wave after being reflected.

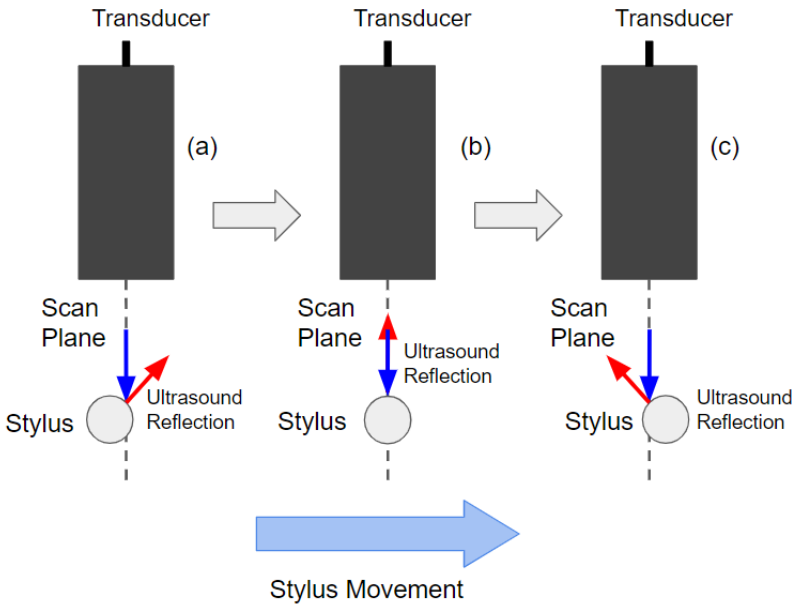

Figure 4.19: Stylus movement.

In both (a) and (c) the ultrasound wave does not hit the stylus in the perpendicular direction, causing the reflected wave to leave the stylus surface with a certain angle relative to the scan plane. In (b)

however, where the stylus is perfectly aligned with the scan plane, the ultrasound wave is reflected parallel to the scan plane. For this reason, it is in (b) that the probe will receive the greater amount of the reflected ultrasound wave causing the stylus to appear much brighter in this image than in the other two. Thus, the total image intensity, obtained by summing the intensity of all the pixels, is a suitable criteria to choose the image.

As in the traditional method, the described procedure was repeated several times, changing the image region where the stylus tip appears, so to constrain a large area of the image. Every image was recorded and a regular intensity pattern is shown in figure 4.20. In this, the stylus was passed trough the scan plane in six different positions. The consecutive peaks with a similar intensity are justified by the fact that the stylus was passed more than once in the same position to assure that suitable alignment was captured.

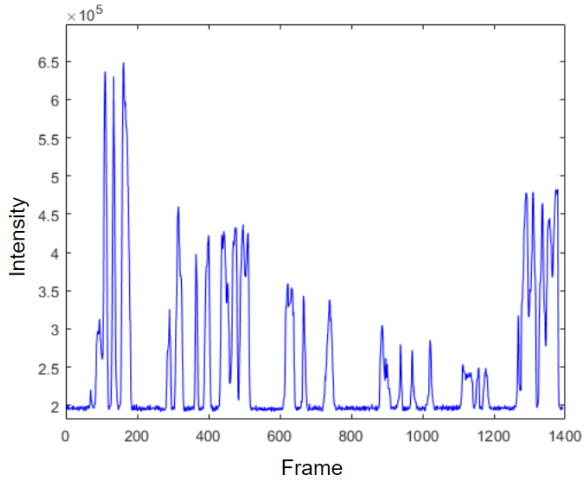

Figure 4.20: Images total intensity.

To find the highest peak captured in each position, the data in figure was filtered by means of a moving average and the resulting signal was divided in groups using an intensity threshold. Briefly, the images were grouped in sets with a filtered intensity above such threshold and the images bellow the threshold were discarded. Finally, the image with the highest total intensity was picked from each group. This is shown in figures 4.21 and 4.22.

Having explained how the image selection was performed, one should now assess the image processing techniques applied to segment the tip of the stylus. First of all, to get a cleaner image of the stylus, the ProSound acoustic power was reduced to 30 %. Also, the region of interest selected was 400×465 pixels while every other machine parameter was kept equal to the ones in section 4.1.2. A regular selected ultrasound frame can be seen in figure 4.23.

The process of finding the stylus tip in the image is divided into segmenting the stylus and then extracting the tip position. Segmenting the stylus was similar to what is described in section 4.1.2, i.e., the image was filtered with a gaussian filter, a threshold was applied and the largest connected component was kept. Then, the tip was selected as the segmented pixel in the lowest row or as the mean among the segmented pixels in the lowest row. Figure 4.24 shows the output of the described

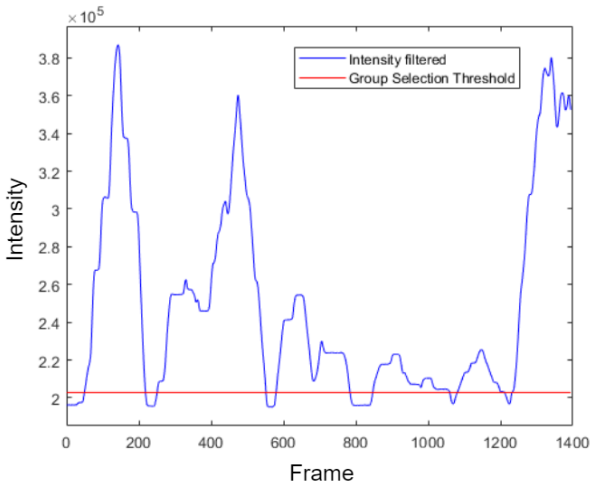

Figure 4.21: Image groups.

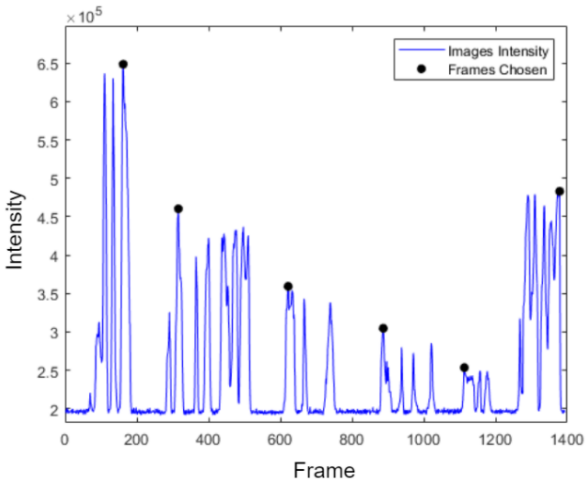

Figure 4.22: Frames chosen.

Figure 4.23: Selected frame.

Figure 4.24: Segmented tip.

procedure.

Finally, the coordinate transformation between the ultrasound image and the flange reference frames can be estimated. The stylus tip position was converted to the flange reference frame, with equation 4.6.

$$p_{Tip}^{Flange} = T_{Base}^{Flange} \cdot T_{Polaris}^{Base} \cdot T_{Stylus}^{Polaris} \cdot p_{Tip}^{Stylus} \tag{4.6}$$

On the other hand, each segmented pixel was converted to millimeters as equation 4.7 shows.

$$p_{Tip}^{Ultrasound} = \begin{bmatrix} {}^{US}s_x & 0 & 0 & 0 \\ 0 & {}^{US}s_y & 0 & 0 \\ 0 & 0 & 0 & 0 \\ 0 & 0 & 0 & 1 \end{bmatrix} \begin{bmatrix} {}^{US}px_{Tip,i} \\ {}^{US}px_{Tip,j} \\ 0 \\ 1 \end{bmatrix} \tag{4.7}$$

Equation 4.5 can, now, be converted in 4.8. This is a typical point-pair registration problem, which can be solved through a least squares minimization which will be assessed in detail in section 4.3.3.

$$\sum_i \left\| p_{Tip,i}^{Flange} - T_{Ultrasound}^{Flange} p_{Tip,i}^{Ultrasound} \right\| \tag{4.8}$$

Finally, figure 4.25 shows the calibration procedure being performed in the laboratory.

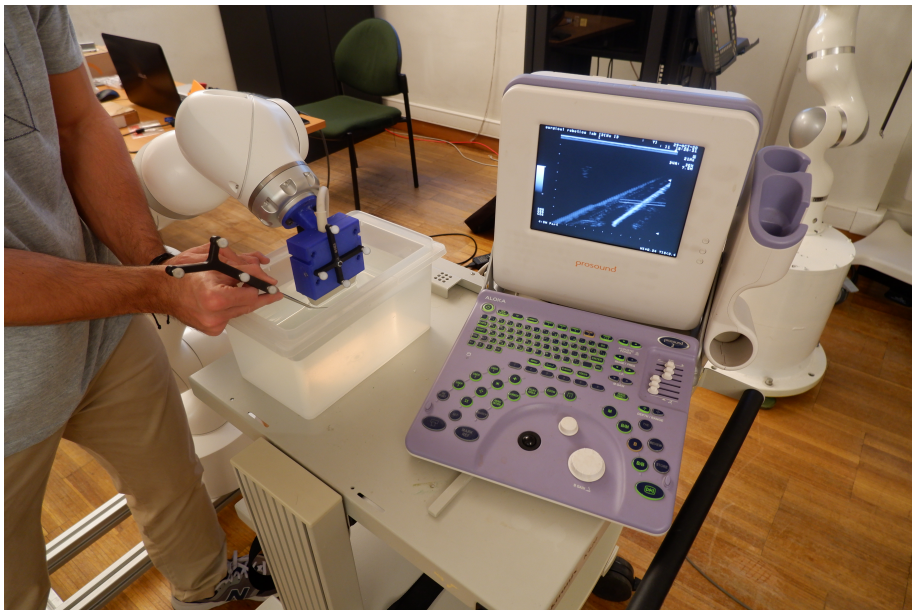

Figure 4.25: Ultrasound calibration procedure.

4.2.4 Needle Calibration

The needle calibration consists in estimating the coordinate transformation between the needle frame of reference and the robot flange or the needle tracker.

An interesting particularity about this frame is that neither the X nor the Y axis orientation are important and thus, it is only needed to find a way to accurately estimate the frame origin position and the orientation of the Z axis.

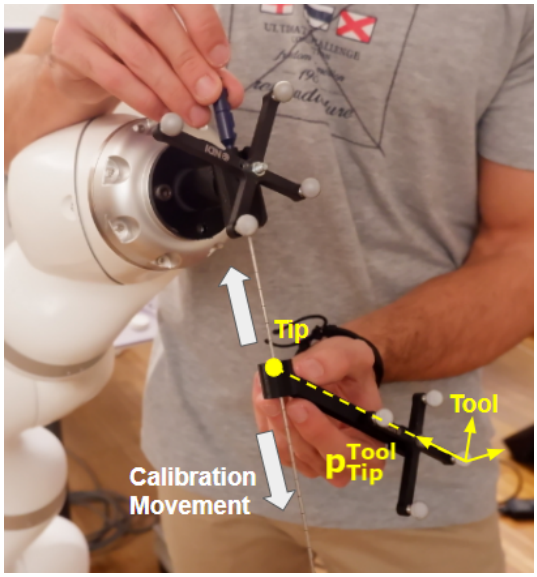

Figure 4.26: Needle calibration.

The calibration was performed as shown in figure 4.26. A calibrating tool was built, allowing a Polaris tracker to be mounted on one end, and with an hole on the other so to slide it along the needle. The tip, highlighted in the figure, is placed in the center of such hole in the outermost surface of the tool and its

position, p_{Tip}^{Tool}, was determined using the stylus.

By sliding the tool along the physical needle, a set of points, collinear with the physical needle, was acquired and an optimization problem was formulated. Note that, since the needle is not completely stiff, it deflects during the process. Furthermore as the calibrating tool was built through 3D printing, a certain slack existed between the tool hole and the needle. Thus, performing the calibration with a simple linear regression would be inaccurate.

The points acquired with the calibrating tool can be transformed to the needle reference frame through equation 4.9 or 4.10, whether one desires to estimate the transformation between the needle and the tracker, or the transformation between the needle and the flange frames of reference.

$$\begin{bmatrix} x_{Needle} \\ y_{Needle} \\ z_{Needle} \\ 1 \end{bmatrix} = T_{Tracker}^{\prime Needle} \cdot T_{Polaris}^{Tracker} \cdot T_{Tool}^{Polaris} \cdot p_{Tip}^{Tool} \tag{4.9}$$

$$\begin{bmatrix} x_{Needle} \\ y_{Needle} \\ z_{Needle} \\ 1 \end{bmatrix} = T_{Flange}^{\prime Needle} \cdot T_{Base}^{Flange} \cdot T_{Polaris}^{Base} \cdot T_{Tool}^{Polaris} \cdot p_{Tip}^{Tool} \tag{4.10}$$

Since the points acquired are supposed to be placed along the Z axis, both x_{Needle} and y_{Needle} should be equal to zero. Also, the transformations $T_{Tracker}^{\prime Needle}$ and $T_{Flange}^{\prime Needle}$ constrain the Z axis but not the frame origin. For that reason, these have only 4 important parameters: the rotation θ_x, the rotation θ_y, the translation d_x and the translation d_y. Since the X and Y axes orientation is not important, the rotation θ_z can be assumed to be zero. Also, the translation d_z will be determined after the optimization to fix the frame origin position. The cost function for such optimization problem can be built as shown in equation 4.11. This was solved in Matlab using the Levenberg-Marquardt method.

$$J(\theta_x, \theta_y, d_x, d_y) = \sum_i \left(x_{Needle,i}^2(\theta_x, \theta_y, d_x, d_y) + y_{Needle,i}^2(\theta_x, \theta_y, d_x, d_y) \right) \tag{4.11}$$

Note that equation 4.11 simply fits a line to the acquired data. This, in turn, is collinear to the Z axis. The frame origin can finally be determined through a simple procedure. The sliding motion begins with the tool tip touching the needle holder surface. So, after the optimization is concluded, the translation d_z is determined so that the origin is coincident with the first points acquired.

4.3 Registration

As stated in section 2.2.3, the registration is the process of estimating the coordinate transformation between two reference frames. These reference frames will be called fixed and moved such that the estimated transformation is the one that transforms the coordinates in the moved reference frame to coordinates in the fixed reference frame. The same way, when point clouds are used, these will also be called fixed and moved such that the estimated transformation is the one that registers the moved point cloud to the fixed point cloud.

Having said so, in this section, the registration algorithms used will be presented.

The most widely used algorithm to solve the point cloud registration problem is the Iterative Closest Point (ICP), proposed by Besl and McKay [45], and improved throughout the years [46–48].

Different approaches to solve this problem also exist in the literature, for instance, [49, 50] present registration algorithms based on the Kalman Filter and [51] developed a method based on the Gaussian mixture model.

These methods have one issue in common. They are sensitive to the initial alignment between the clouds. Thus, authors in [52–54] propose a coarse registration step to provide good initial conditions to the aforementioned algorithms.

In this work two different approaches were attempted. The first approach consisted in performing an initial coarse alignment using the Principal Component Analysis (PCA), [53, 54], followed by a fine registration step with the ICP algorithm. On the other hand, in the second approach, an iterative algorithm was developed to register the clouds based on the local Gauss and mean curvatures.

In section 3.5, a methodology to evaluate how the error propagates is presented. This consists in performing three registration steps, namely, the CT to ground truth, the ultrasound to ground truth and the CT to ultrasound. Having said so, these three steps were accomplished in the following way:

1. In the first step, CT to ground truth, the CT point cloud will be the moved one and the ground truth point cloud will be the fixed one. The moved point cloud will be initially transformed using the transformation $T_{CT}^{\prime Base}$, calculated through the targets registration, section 3.5, to achieve a suitable initial alignment. This is the transformation that best aligns the targets but not necessarily the one that best aligns the point clouds. Then, the transformed moved point cloud will be registered to the fixed point cloud using the ICP so to calculate the error on the targets when the clouds are best aligned.

2. In the second step, ultrasound to ground truth, the ultrasound point cloud will be the moved point cloud and, once again, the ground truth point cloud will be the fixed one. There is no need to apply an initial transformation in this case because the clouds should be sufficiently well aligned in their original positions. The registration will be performed solely by applying the ICP.

3. In the third and main step, CT to ultrasound, the CT point cloud will be the moved point cloud and the ultrasound will be the fixed point cloud. To perform this step, the algorithms described in this section will be used. This is the only step to be performed in a real application and only in this step

will the performance associated to the algorithms be evaluated. The previous two steps are used merely to assess which sources of error exist and how they influence the final result.

4.3.1 PCA and ICP

To start with, the principal components of each point cloud were calculated and then the coarse registration was estimated by aligning these. The output of such procedure is a coordinate transformation which brings the moved point cloud to a position where it is coarsely aligned with the fixed point cloud. Finally, the ICP was applied, having as input, the transformed moved point cloud and the fixed point cloud.

PCA Coarse Registration

The Principal Component Analysis is a dimensionality reduction technique widely used in statistics. It creates an hierarchical coordinate system that represents the variations in the data set.

A two-dimensional example is presented in figure 4.27, where it is possible to see a data set and its principal components.

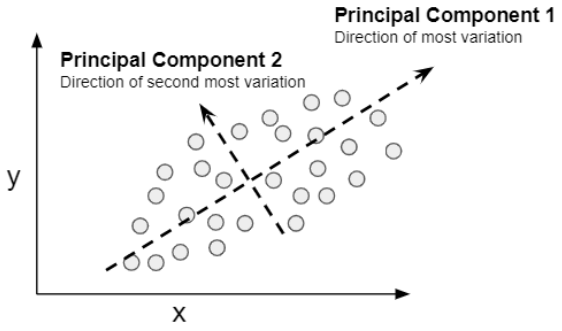

Figure 4.27: Principal Components in 2D.

The principal components of a data set can be computed through the eigenvalue decomposition of its mean centered form covariance matrix. Consider the data set S, a point cloud of *n* points, of the form 4.12.

$$S = \begin{bmatrix} s_1 \\ s_2 \\ \vdots \\ s_n \end{bmatrix} = \begin{bmatrix} x_1 & y_1 & z_1 \\ x_2 & y_2 & z_2 \\ \vdots & \vdots & \vdots \\ x_n & y_n & z_n \end{bmatrix} \tag{4.12}$$

The first step is to build the mean centered point cloud, B, obtained by subtracting the mean matrix, $\bar{S}$, to the original point cloud. The mean matrix is given by equation 4.13.

$$\bar{S} = \begin{bmatrix} 1 \\ 1 \\ \vdots \\ 1 \end{bmatrix} \cdot \bar{s} \tag{4.13}$$

Where $\bar{s}$ is the centroid of S:

$$\bar{s} = \frac{1}{n}\sum_{j=1}^{n}[x_j \ y_j \ z_j] \tag{4.14}$$

The mean centered point cloud, B, can now computed as shown in equation 4.15.

$$B = S - \bar{S} \tag{4.15}$$

The covariance matrix can be obtained with 4.16.

$$C = B^T \cdot B \tag{4.16}$$

This a 3×3 matrix that can be decomposed into eigenvalues and eigenvectors, equation 4.17.

$$C = V \cdot D \cdot V^T \tag{4.17}$$

Consider now a fixed point cloud, F, constituted by the points f_i, and a moved point cloud, M, constituted by the points m_i, of the form of 4.12. Also, each point f_i is determined by applying a rigid coordinate transformation to each point m_i, equation 4.18. Let V_F and V_M be the principal components matrices of the fixed and moved point clouds respectively.

$$f_i = (R \cdot m_i^T + t)^T \ \ \forall \ \ f_i \in F \ , \ m_i \in M \tag{4.18}$$

Therefore the principal components of the fixed point cloud will be the principal components of the moved point cloud rotated by the matrix R, as shown in equation 4.19.

$$V_F = R \cdot V_M \tag{4.19}$$

The coordinate transformation that transforms M in F can be calculated following two simple steps. The first is to compute the rotation matrix, R, which can be calculated through equation 4.20.

$$R = V_F \cdot V_M^T \tag{4.20}$$

Finally, let $\bar{f}$ and $\bar{m}$ be the the centroids of the fixed and the moved point clouds. The translation vector, t, is given by 4.21.

$$t = \bar{f}^T - R \cdot \bar{m}^T \tag{4.21}$$

ICP Fine Registration

The Iterative Closest Point is a method to register two point clouds using the geometric position of their constituent points. This problem can be divided in two separate tasks which are: finding the correspondence between the points, i.e., which point of the fixed point cloud corresponds to a given

point of the moved point cloud, and compute the coordinate transformation that transforms each point in the moved point cloud to its correspondent point in the fixed point cloud.

The ICP performs this two tasks in an iterative manner, which can be divided in three steps, that repeat until a stopping criterion is met:

1. For each point of the moved point cloud, the correspondent point in the fixed point cloud is the closest one.

2. Find the transformation that transforms each point of the moved point cloud to its correspondent point in the fixed point cloud by means of a point-pair registration.

3. Apply the estimated transformation to the moved point cloud.

The Matlab implementation of the algorithm was used with the point to point minimization metric. This was chosen since it provides better results with less iterations and processing time for the specific case in study, [1].

Finally, the most suitable stopping criterion is the stagnation of the registration residue. This is given by the mean euclidean distance between each moved point and its correspondent fixed point.

4.3.2 Curvature-Based Registration

Just like the ICP algorithm, the method proposed here will divide the registration problem in two tasks, i.e., finding the correspondence between points and calculate the coordinate transformation that transforms each point of the moved cloud to the correspondent point of the fixed cloud.

The description of each point by means of its Gaussian and mean curvatures will be used to, together with the euclidean distance, decide the best correspondence between the points of both clouds. This way, the final registration is expected to be more accurate than the one achieved using the ICP.

Gauss and Mean Curvatures

The Gaussian curvature, K_G, and the mean curvature, K_H, are the typical way to represent the curvature of a surface. These are calculated through the principal curvatures, k_1 and k_2, which in turn, are the maximum and the minimum normal curvatures of a surface at a given point.

Having said so, consider the surface S and the point V belonging to that surface, figure 4.28. The principal curvatures of the surface S passing through V are associated with the curves C_1 and C_2 in the normal directions e_1 and e_2. Furthermore, there is an infinite set of curves in S passing through V. By definition the curvature is the reciprocal of the radius of the circle that best fits a given curve in a given point. For example the curvature of the curve C_n can be calculated through the reciprocal of R_n. Finally, the Euler curvature equation, shown in 4.22 relates the curvature of a generic curve passing through V with its principal curvatures.

$$k_n = k_1 cos^2(\theta) + k_2 sin^2(\theta) \tag{4.22}$$

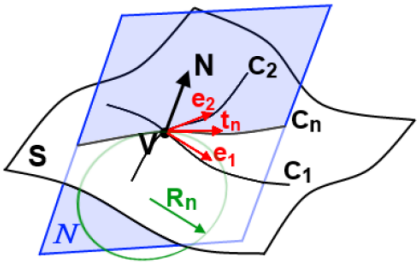

Figure 4.28: Curvatures at point V. (From [33])

Where θ is the angle between the tangent direction t_n and the direction e_1, figure 4.29.

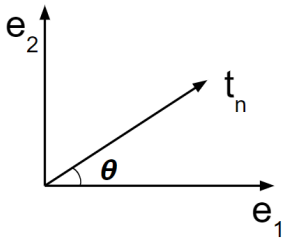

Figure 4.29: Curvature directions.

Having explained the mathematical meaning of surface curvatures in a point, one will now explain how the these were estimated numerically for a point cloud. This estimation is divided into three main steps, following the procedure in [55].

To start with, one must calculate the surface normal in every point P of a given point cloud, of the form 4.23. To achieve this, the estimation of the tangent plane, [56], was performed.

$$P = \begin{bmatrix} x_P \\ y_P \\ z_P \end{bmatrix} \tag{4.23}$$

In [56] a method is proposed which consists in representing the tangent plane, $Tp(P)$, of P with a center point O and a unit normal vector N. Also, a neighborhood of the point P is defined so to contain the k nearest neighbours of such point and is represented by $Nhbd(P)$. Thus, the position of O is calculated as the centroid of $Nbhd(P)$, and the N is calculated through a principal component analysis of $Nbhd(P)$. Having said so, the covariance matrix of $Nbhd(P)$ was built as shown in equation 4.24.

$$CV = \sum_{Q \in Nbhd(P)} (Q - O) \cdot (Q - O)^T \tag{4.24}$$

The matrix CV was then decomposed in eigenvalues, $\lambda^1 > \lambda^2 > \lambda^3$, and the respective eigenvectors, ν^1, ν^2 and ν^3. The first two eigenvectors, ν^1 and ν^2, are coplanar to $Tp(P)$ and N is parallel to ν^3. To assure that the normal vector in each point is coherently aligned with the others, pointing outside of the point cloud, the centroid of the entire point cloud, $\bar{P}$, was computed. The normal vector was defined as shown in 4.25.

$$N = \begin{cases} \nu^3 & if \quad (P - \bar{P})^T \cdot \nu^3 \geq 0 \\ -\nu^3 & if \quad (P - \bar{P})^T \cdot \nu^3 < 0 \end{cases} \tag{4.25}$$

The second step was to estimate every curvature k_n^i passing through P. Here one used the set of points Q_i belonging to a neighborhood of P, different from the previous $Nbhd(P)$. The new neighborhood was defined as the set of points Q_i, that hold equation 4.26 where d is an arbitrary small value.

$$\|Q_i - P\| < d \tag{4.26}$$

Also, let N be defined by $[n_x, n_y, n_z]$ and let $\{P, X, Y, N\}$ be a local coordinate system, figure 4.30, such that, X and Y are orthogonal unit vectors and can be calculated through equations in 4.27.

$$\begin{aligned} \phi &= atan(n_y, n_x) \\ Y &= [-sin(\phi), \ \ cos(\phi), \ \ 0] \\ X &= Y \times N \end{aligned} \tag{4.27}$$

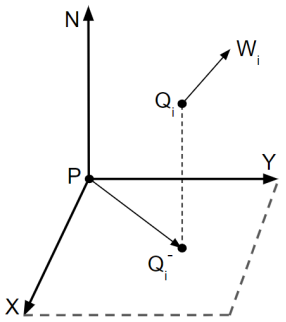

Figure 4.30: Local coordinate system.

In this coordinate system, P is defined by $[0, 0, 0]$ and Q_i by $[x_i, y_i, z_i]$. Also, Q_i^- represents the projection of Q_i in the pane XY and is defined by $[x_i, y_i, 0]$. On the other hand, W_i is the surface normal in the point Q_i and is defined in the local coordinate system by $[w_{x,i}, w_{y,i}, w_{z,i}]$.

Having said so, the problem of computing k_n^i is given in 2D as shown in figure 4.31 where the the curvature is calculated through 4.28.

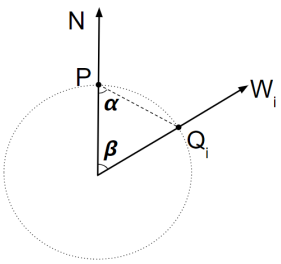

Figure 4.31: 2D Curve.

$$k_n^i = \frac{sin(\beta)}{\|P - Q_i\| \, sin(\alpha)} \tag{4.28}$$

This, however, only holds for the case in which the the normal vectors N and W_i are coplanar, which is rarely the case for 3D point clouds. Some approximations will then be made to transform our 3D problem in 2D. First of all, for every point Q_i, in the neighborhood of P, z_i is approximately zero. Thus, one will assume that z_i is indeed zero which reduces Q_i to Q_i^-. The normal vector W_i is then decomposed in two components, one parallel to N and other parallel to the vector $P\vec{Q}_i^-$.

$$W_{i,\ N||} = w_{z,i} \tag{4.29}$$

$$W_{i,\ P\vec{Q}_i^-||} = w_{xy} = \frac{w_{x,i} \cdot x_i + w_{y,i} \cdot y_i}{\sqrt{x_i^2 + y_i^2}} \tag{4.30}$$

This approximation is shown in figure 4.32 where W^- is a reduction of W to 2 dimensions.

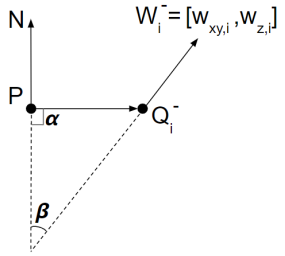

Figure 4.32: 2D Approximation.

Finally, one can write equation 4.28 as 4.31.

$$k_n^i = \frac{w_{xy,i}}{\sqrt{x_i^2 + y_i^2} \cdot \sqrt{w_{xy,i}^2 + w_{z,i}^2}} \tag{4.31}$$

Which is obtained by making the substitutions of 4.32 to 4.35.

$$\alpha = 90^\circ \rightarrow sin(\alpha) = 1 \tag{4.32}$$

$$sin(\beta) = \frac{w_{xy,i}}{|W^-|} \tag{4.33}$$

$$\left|W^-\right| = \sqrt{w_{xy,i}^2 + w_{z,i}^2} \tag{4.34}$$

$$\|P - Q_i\| = \sqrt{x_i^2 + y_i^2} \tag{4.35}$$

The third step for estimating the principal curvatures was a least squares optimization with the Euler curvature equation. One can write the Euler curvature equations as 4.36.

$$k_n^i = k_1\ cos^2(\theta_i + \theta) + k_2\ sin^2(\theta_i + \theta) \tag{4.36}$$

Where the unknown parameters are θ, k_1 and k_2. By the definition employed, θ is the angle between e_1 and X, and θ_i is the angle between the vector $P\vec{Q}_i^-$ and X. To make it clear, figure 4.33 shows the plane XY and how these angles are defined.

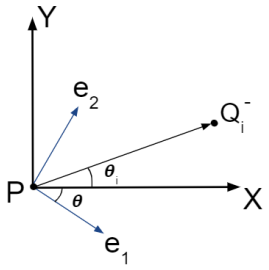

Figure 4.33: *XY* Plane.

Equation 4.36 can be written as a minimization for all the points, Q_i, in the neighborhood of P as in 4.37.

$$\min_{k_1,k_2,\theta} \sum_i \left[k_1\ cos^2(\theta_i+\theta) + k_2\ sin^2(\theta_i+\theta) - k_n^i\right]^2 \tag{4.37}$$

Equation 4.37 can be decomposed as shown in 4.38 and thus the matrix form shown in 4.39 can be written.

$$\begin{aligned} k_1\ cos^2(\theta_i+\theta) + k_2\ sin^2(\theta_i+\theta) = cos^2(\theta_i)\cdot(k_1\ cos^2(\theta) + k_2\ sin^2(\theta)) \\ +2\ cos(\theta_i)\ sin(\theta_i)\cdot(k_2\ cos(\theta)sin(\theta) - k_1\ cos(\theta)sin(\theta)) \\ +sin^2(\theta_i)\cdot(k_1\ sin^2(\theta) + k_2\ cos^2(\theta)) \end{aligned} \tag{4.38}$$

$$\min_{\mu} \|A\cdot u - B\|^2 \tag{4.39}$$

Where A, u and B are given by 4.40. On the other hand, C, D and E are given by 4.41 and result from the minimization of 4.39.

$$A_{w\times 3} = \begin{bmatrix} cos^2(\theta_1) & 2cos(\theta_1)sin(\theta_1) & sin^2(\theta_1) \\ \vdots & \vdots & \vdots \\ cos^2(\theta_i) & 2cos(\theta_i)sin(\theta_i) & sin^2(\theta_i) \\ \vdots & \vdots & \vdots \\ cos^2(\theta_n) & 2cos(\theta_n)sin(\theta_n) & sin^2(\theta_n) \end{bmatrix}, \ u = \begin{bmatrix} C \\ D \\ E \end{bmatrix}, \ B_{w\times 1} = \begin{bmatrix} k_n^1 \\ \vdots \\ k_n^i \\ \vdots \\ k_n^w \end{bmatrix} \tag{4.40}$$

$$\begin{aligned} C &= k_1\ cos^2(\theta) + k_2\ sin^2(\theta) \\ D &= (k_2 - k_1)\cdot cos(\theta)sin(\theta) \\ E &= k_1\ sin^2(\theta) + k_2\ cos^2(\theta) \end{aligned} \tag{4.41}$$

Finally, one can build the matrix Θ. As shown in equation 4.42 the principal curvatures, k_1 and k_2

are given by the eigenvalues of Θ while the principal curves direction, e_1 and e_2, are given in the local coordinate system by the eigenvectors.

$$\Theta = \begin{bmatrix} C & D \\ D & E \end{bmatrix} = \begin{bmatrix} k_1\ cos^2(\theta) + k_2\ sin^2(\theta) & (k_2 - k_1) \cdot cos(\theta) sin(\theta) \\ (k_2 - k_1) \cdot cos(\theta) sin(\theta) & k_1\ sin^2(\theta) + k_2\ cos^2(\theta) \end{bmatrix} = \begin{bmatrix} cos(\theta) & sin(\theta) \\ -sin(\theta) & cos(\theta) \end{bmatrix} \cdot \begin{bmatrix} k_1 & 0 \\ 0 & k_2 \end{bmatrix} \cdot \begin{bmatrix} cos(\theta) & -sin(\theta) \\ sin(\theta) & cos(\theta) \end{bmatrix} \tag{4.42}$$

The Gauss and mean curvatures were, then, calculated through 4.43.

$$K_G = k_1 \cdot k_2 \ \ , \ \ K_H = \frac{k_1 + k_2}{2} \tag{4.43}$$

Registration

Having the Gauss and mean curvatures calculated for each point in the point clouds, a registration algorithm must now be designed. In sum, the designed method uses the euclidean distance to define the set of fixed points that can be matched to a moved point, i.e., a given moved point, m_j, can be matched to any fixed point, f_k, such that equation 4.44 holds.

$$\|m_j - f_k\| < R \tag{4.44}$$

Then, it uses the estimated curvatures to find the best match within the neighborhood radius R, that is, the point f_k, holding 4.44, that solves equation 4.45.

$$f_{match,j} = \underset{f_k}{argmin}(\ |K_G(f_k) - K_G(m_j)|\ +\ |K_H(f_k) - K_H(m_j)|\ ) \tag{4.45}$$

Where $K_G()$ and $K_H()$ define, respectively, the Gauss and mean curvatures of a given point. Finally, a point-pair registration problem is formulated to compute the transformation T_i that best transforms every point m_j to its match. This is shown, in homogeneous coordinates, in equation 4.46, and the solution can be found through a least-squares optimization, section 4.3.3.

$$\sum_j \|f_{match,j} - T_i \cdot m_j\| \tag{4.46}$$

At the end of each iteration, this transformation is applied to the moved point cloud, changing the position of every point m_j, and the value of R is decreased, using equation 4.47. In this, C is an arbitrary small constant, R_0 is the initial value of R, R_{min} is the minimum allowed value of R and i is the iteration.

$$R_i = max(R_0 \cdot e^{-C \cdot (i-1)}\ , R_{min}) \tag{4.47}$$

This procedure works under the assumption that the point $f_{match,j}$, that represents the best match

to the point m_j, is in its vicinity. However, two things may happen that cause this to not be the case.

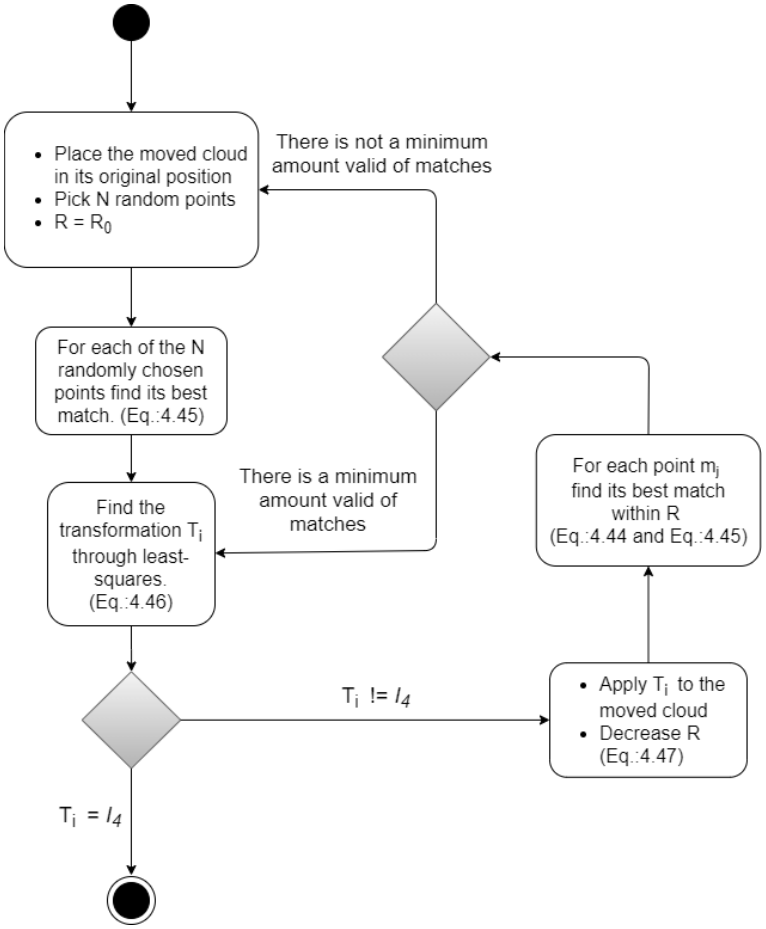

Figure 4.34: Registration algorithm.

In the first iteration the moved cloud is in a random position relative to the fixed cloud. In this case, the aforementioned assumption is obviously wrong. For that reason, in the first iteration, the best match to every point m_j is searched through the entire fixed cloud, neglecting the distance condition of equation 4.44. This, however, leads to the second problem.

The estimated curvature for the same theoretical point in the CT point cloud and in the ultrasound point cloud may differ. Consequently, solving equation 4.45 with no neighborhood radius condition may result in a wrong matching which leads to a wrong alignment.

When the moved point cloud is transformed with a wrong coordinate transformation, at some iteration, some of the moved points will not have any fixed point in its vicinity, causing the algorithm to get stuck.

For this reason, the first iteration is only performed using N randomly chosen points and, whenever the algorithm gets stuck, the moved points with no neighbours within R are neglected. However, this is done only as long as there is a minimum amount of valid matches. When this minimum is not achieved, it is assumed that the N points chosen for the first iteration failed to give a suitable alignment. Thus the algorithm will restart, placing the moved point cloud in its original position and picking a new set of N initial points. Figure 4.34 shows a diagram which represents this algorithm schematically.

4.3.3 Point-Pair Registration

The problem of registering two point sets with known correspondences can be formulated as an optimization problem with the cost function shown in 4.48, using Cartesian coordinates.

$$\sum_{i=1}^{n} \|R \cdot m_i + t - f_i\| \tag{4.48}$$

Where m_i is a moved point and f_i is the correspondent fixed point. Also R is the rotation matrix and t is the translation vector.

Arun et al. [57] proposes a stepwise method to minimize such cost function. Assume that $\bar{m}$ and $\bar{f}$ represent the centroid of the moved and the fixed point sets, respectively. Also assume that both the moved and the fixed point sets, M and F, are defined as shown in 4.49.

$$M = \begin{bmatrix} m_1 & \dots & m_n \end{bmatrix} = \begin{bmatrix} x_1 & \dots & x_n \\ y_1 & \dots & y_n \\ z_1 & \dots & z_n \end{bmatrix} \ , \ F = \begin{bmatrix} f_1 & \dots & f_n \end{bmatrix} = \begin{bmatrix} x_1 & \dots & x_n \\ y_1 & \dots & y_n \\ z_1 & \dots & z_n \end{bmatrix} \tag{4.49}$$

The method can be divided in five steps:

1. Compute the centered point sets, M' and F', by subtracting the centroids to each point set.

$$M' = M - \bar{m} \cdot \begin{bmatrix} 1 & \dots & 1 \end{bmatrix} \ , \ F' = F - \bar{f} \cdot \begin{bmatrix} 1 & \dots & 1 \end{bmatrix} \tag{4.50}$$

2. Compute the 3×3 matrix H given by:

$$H = F' \cdot M'^T \tag{4.51}$$

3. Compute the singular value decomposition of H:

$$H = U \cdot \Lambda \cdot V^T \tag{4.52}$$

4. The rotation matrix R is given by:

$$R = V \cdot U^T \tag{4.53}$$

5. Finally, the translation vector can be calculated through:

$$t = \bar{f} - R \cdot \bar{m} \tag{4.54}$$

4.3.4 Implementation

The ultrasound imaging was performed so to acquire the maximum amount of the phantom surface, thus, the forehead and both the right and left sides of the phantom were imaged. Figure 4.35 shows one example of a regular point cloud built from ultrasound images.

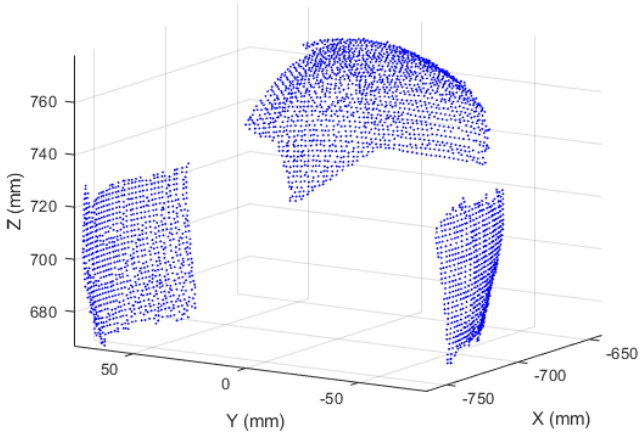

Figure 4.35: Ultrasound point cloud in the robot base reference frame.

Principal Component Analysis

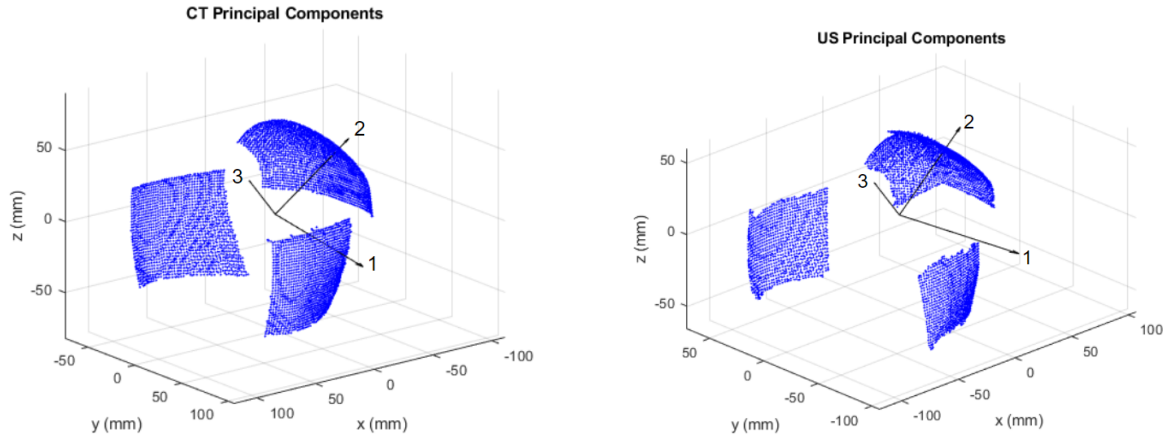

(a) (b)

Figure 4.36: Principal Components of CT point cloud (a) and of ultrasound point cloud (b).

In order to perform the coarse registration using the principal component analysis, the point clouds must have a similar shape. For that reason, an algorithm was designed to clip the original CT point cloud, figure 4.5, keeping only the forehead and the sides. This procedure does not need to be much accurate and for that reason it can also be performed manually through a suitable GUI, or using 3D Slicer.

The principal components of each point cloud were calculated and can be seen in 4.36. This figures show the mean centered point cloud and the 1^{st}, 2^{nd} and 3^{rd} principal components marked with the respective number.

Mean and Gauss Curvatures

The estimated Gaussian and mean curvatures for both the CT and the ultrasound point clouds can be seen in figures 4.37 and 4.38. These figures show the normalized curvatures so to ease the reader interpretation.

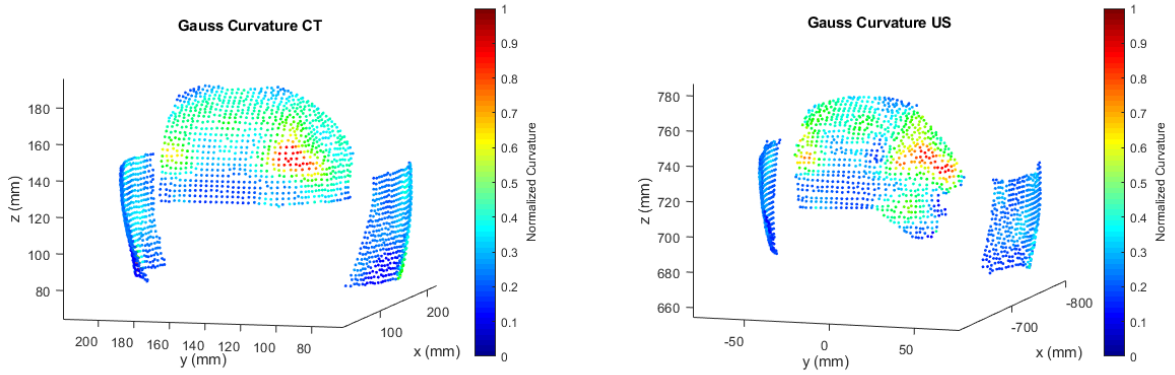

(a) (b)

Figure 4.37: Normalized Gaussian curvature of the CT point cloud (a) and of the ultrasound point cloud (b).

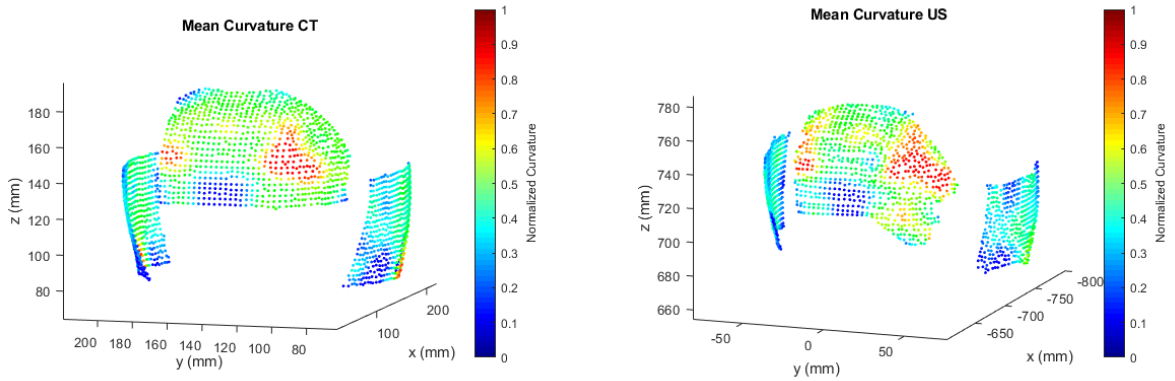

(a) (b)

Figure 4.38: Normalized mean curvature of the CT point cloud (a) and of the ultrasound point cloud (b).

Note that, the curvature-based registration does not require any clip of the CT point cloud. However, the images show clipped CT clouds to favour the visualization.

Chapter 5

Results and Discussion

In this section, the project results will be presented and discussed. Additional tests were performed when necessary and these will also be presented here.

5.1 Calibration

Results Presentation

Starting by the setup calibration procedure, the first important result is associated to the stylus calibration. The results can be seen in table 5.1, where there is shown the mean and the maximum calibration residues. These values were given directly by the NDI software.

Mean Error (mm)	0,42
Max. Error (mm)	1,16

Table 5.1: Stylus pivoting results.

Regarding the Polaris to base calibration, the main result to be assessed is the residue of the least squares optimization of the equation 4.4. Table 5.2 shows the mean, the maximum and the minimum residue as well as the standard deviation of these.

Mean Error (mm)	0,40
Max. Error (mm)	0,88
Min. Error (mm)	0,06
Std. Dev. (mm)	0,17

Table 5.2: Polaris to base calibration results.

As referred in section 3.5, the quality of the ultrasound spatial calibration was assessed by means of the point reconstruction accuracy (PRA), and the calibration reproducibility (CR), which are calculated through equations 3.25 and 3.26. The calibration procedure was repeated 10 times and the results will be presented next.

The PRA was calculated by estimating the position of the tip of a tracked 3D printed cone. This was imaged near the four corners and the center of the image and the result can be seen in table 5.3.

Point	Mean Error (mm)
Upper Left	0,75
Upper Right	1,26
Bottom Left	0,74
Bottom Right	0,87
Center	0,84
Mean	0,89

Table 5.3: PRA results.

As described in section 3.5, the calibration reproducibility is calculated as the standard deviation of the image corners and center position estimation. The results can be seen in table 5.4.

Point	Std. Dev. (mm)
Upper Left	0,34
Upper Right	0,66
Bottom Left	0,40
Bottom Right	0,87
Center	0,41

Table 5.4: CR results.

Finally, the results concerning the needle calibration. The evaluation of the needle calibration quality was performed by calculating the residues of the cost function, equation 4.11, at the solution. These are shown at table 5.5.

Mean Error (mm)	0,64
Max. Error (mm)	3,43
Min. Error (mm)	0,02
Std. Dev. (mm)	0,57

Table 5.5: Needle calibration results.

Also figure 5.1, shows a three dimensional representation of the calibration output, where it is possible to see the position of the points acquired, the fitted line and the needle reference frame.

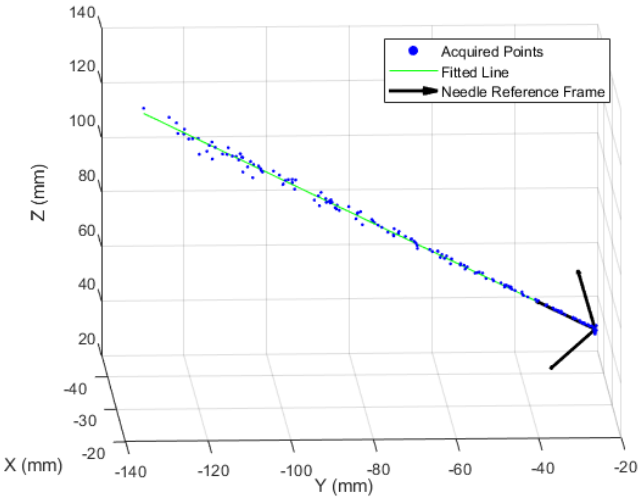

Figure 5.1: Needle calibration shown in the Polaris reference frame.

Discussion

To start with, there is the stylus pivoting calibration. This is the standard way to calculate the stylus tip position and the error associated to this is mainly due to the difficulty in assuring that the tip is completely static throughout the calibration procedure, as it is done by hand. Also, the stylus tip has a diameter of around 1 mm which makes it impossible to calculate a single point that defines it. Consequently, every position measured with the stylus will have a certain degree of uncertainty.

Regarding the Polaris to robot base calibration, an additional experiment was performed to find the source of the error presented in table 5.2. The experiment consisted in commanding the robot to move its flange in a straight line along the X axis with reference to the base frame. This way, the robot got progressively more stretched out moving its center of mass away from the base. The flange position was recorded by the Polaris and the result can be seen in figures 5.2a and 5.2b, where the Polaris points are the flange positions measured by the Polaris, while the robot points are the ones measured by the robot.

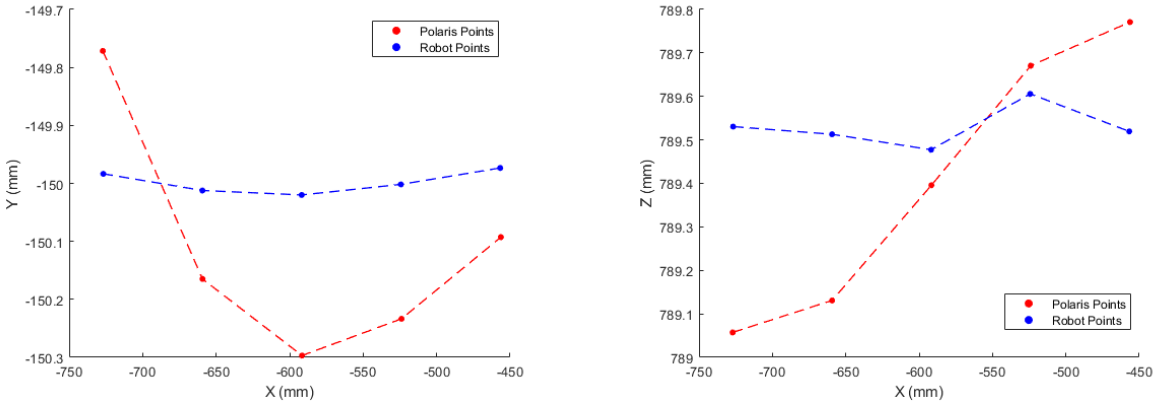

(a) XY Plane

(b) XZ Plane

Figure 5.2: Straight line along X axis.

Note that the Polaris readings show a much higher variance in the flange position than the robot readings. To quantify this difference between the robot and the Polaris readings, equation 5.1 was used.

$$d_{nonrigid} = \|p_{Polaris,f} - p_{Polaris,i}\| - \|p_{Robot,f} - p_{Robot,i}\| \tag{5.1}$$

Where $p_{Polaris,i}$ and $p_{Polaris,f}$ are, respectively, the initial and final positions registered by the Polaris. Similarly, $p_{Robot,i}$ and $p_{Robot,f}$ are, respectively, the initial and final positions registered by the robot. Also, by applying the equation to the data in figures 5.2a and 5.2b, one got $d_{nonrigid} = 0.79\ mm$.

This result show that some non-rigid behaviour is associated to the robot movement, leading to the conclusion that the robot coupling base is deflecting in some way. Consequently, the rigid coordinate transformation that results from this calibration will not fit perfectly. The experiment was repeated performing straight lines along y and z but not other interesting conclusions have been taken.

As for the ultrasound spatial calibration, the results for the accuracy and precision are justified by several reasons. To start with, the whole calibration is performed under the assumption that the stylus is always parallel to the scan plane. However, since the procedure is done by hand, it is impossible to

assure a perfect alignment.

The second reason has to do with the stylus tip and its segmentation. As mentioned, the stylus tip as a diameter of around 1 mm. On the other hand, the ultrasound image resolution is around 0.1 mm in both directions. Thus, it is impossible to find a single pixel which corresponds to stylus tip with no uncertainty. Nevertheless, the error introduced by both these issues can be attenuated by using more points to calibrate.

Finally, there is the needle calibration. The calibration results shown in table 5.5 are the residues of the minimization of equation 4.11 and are caused by the two factors mentioned in section 4.2.4, that are, the needle deflection and the slack between the needle and the calibration tool hole. Also, these results are from the $T_{Tracker}^{Needle}$ and T_{Flange}^{Needle} estimations as both were estimated through the same set of points. Further validation for this calibration was merely visually performed, for instance by commanding the robot to align the needle with the vertical or horizontal axes.

5.2 Registration

Results Presentation

In this section, the results of the registration process will be presented. To start with, there is the targets acquisition and the determination of the ground truth transformation, $T_{CT}^{'Base}$.

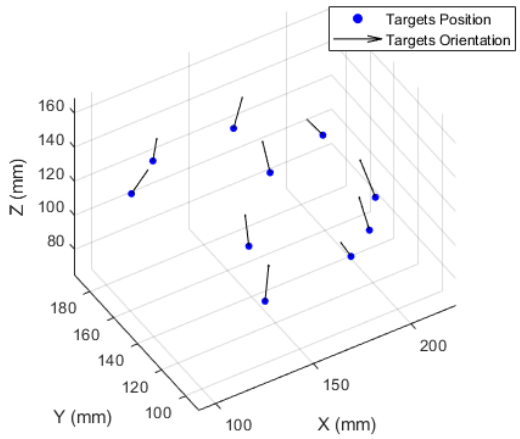

Figure 5.3: Segmented targets in CT reference frame.

Regarding the targets segmentation in the CT, figure 5.3 shows the segmented position and orientation of the these in the CT reference frame.

The targets were acquired in the laboratory and registered to the CT targets as explained in section 3.5 to compute the ground truth transformation. Table 5.6 show the result of this procedure.

Finally, the targets orientation in the base reference frame was estimated through equation 3.7 and figure 5.4 show the position and orientation of the targets in the robot base reference frame.

The ground truth point cloud was acquired and the first step of the registration, the CT to ground

Target	e_p (mm)
1	0,56
2	0,65
3	0,51
4	0,79
5	0,69
6	0,59
7	0,18
8	0,77
9	0,54
10	0,86
Mean	0,61

Table 5.6: Targets registration residue.

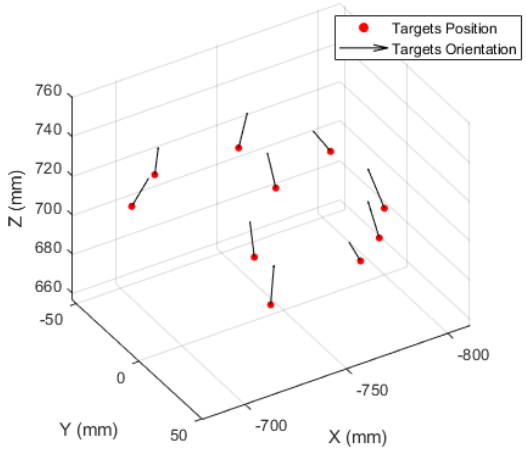

Figure 5.4: Acquired targets in the robot base reference frame.

truth, was performed. The results of this can be seen in table 5.7.

Target	e_p (mm)	e_v (°)
1	0,69	0,14
2	0,49	0,15
3	0,93	0,19
4	0,62	0,16
5	1,16	0,09
6	0,82	0,19
7	0,74	0,15
8	0,87	0,14
9	0,85	0,10
10	1,30	0,10
Mean	0,85	0,14

Table 5.7: CT to ground truth registration error.

To perform the second and third steps of the stepwise error evaluation described in section 3.5, 10 different ultrasound scans were made. The second step, ultrasound to ground truth, results can be seen in table 5.8. Also, the error distribution for each target is shown in figures 5.5a and 5.5b.

The third step was then performed. The first attempt to perform this used the PCA + ICP method.

Target	e_p (mm)		e_v (°)	
	Mean	Std. Dev.	Mean	Std. Dev.
2	0,62	0,14	0,42	0,20
3	0,67	0,15	0,40	0,19
4	0,75	0,19	0,40	0,20
5	0,62	0,19	0,37	0,17
6	0,76	0,25	0,4	0,19
7	0,77	0,23	0,42	0,20
8	0,57	0,20	0,42	0,20
9	0,67	0,24	0,39	0,18
10	0,52	0,20	0,40	0,19
Mean	0,66	0,15	0,40	0,19

Table 5.8: Ultrasound to ground truth registration accuracy.

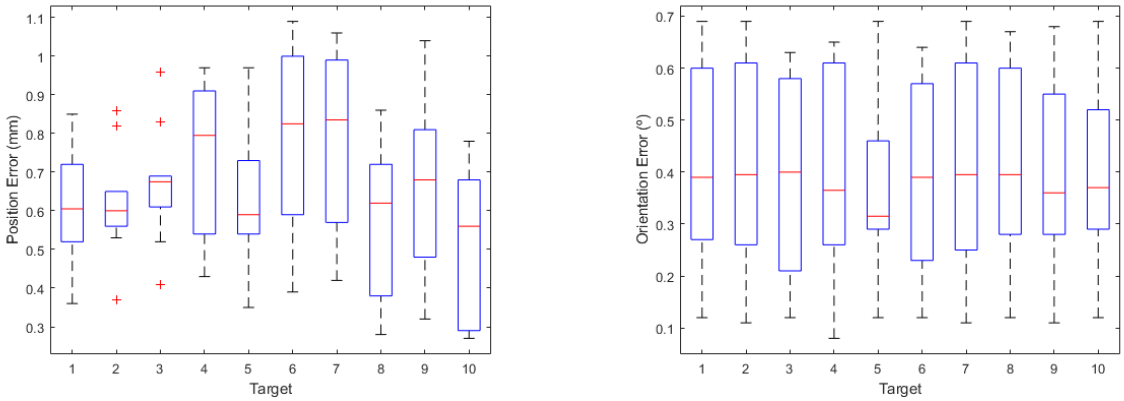

(a) Position error

(b) Orientation error

Figure 5.5: Ultrasound to ground truth target error distribution.

The results are presented in table 5.9 and in figures 5.6a and 5.6b.

Target	e_p (mm)		e_v (°)	
	Mean	Std. Dev.	Mean	Std. Dev.
1	3,12	0,45	4,99	1,07
2	4,43	1,04	4,98	1,06
3	5,44	1,63	5,21	0,95
4	7,28	1,38	3,73	1,00
5	3,28	0,88	4,97	1,11
6	6,04	1,04	5,14	0,90
7	6,81	1,22	4,84	1,06
8	2,45	0,80	5,17	0,97
9	2,32	0,58	4,60	1,19
10	3,44	0,78	5,10	1,02
Mean	4,46	0,73	4,87	1,00

Table 5.9: PCA + ICP registration accuracy.

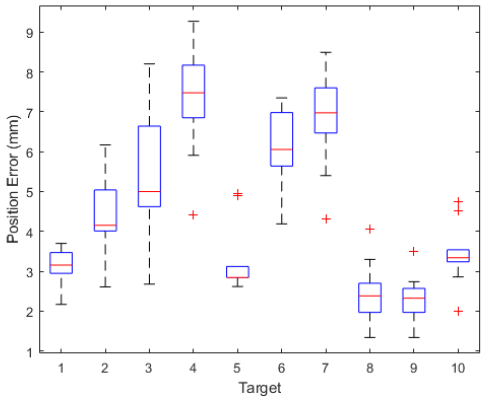

(a) Position error

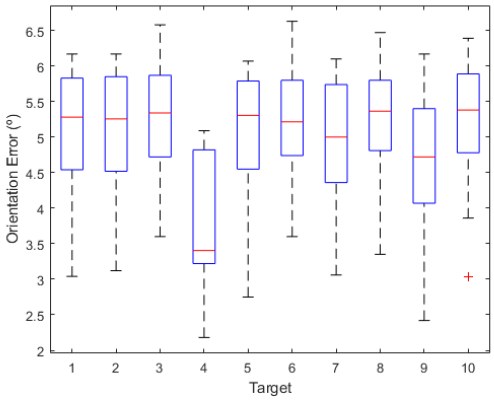

(b) Orientation error

Figure 5.6: PCA + ICP target error distribution.

The curvature-based algorithm was also applied and the results are shown in table 5.10 and figures 5.7a and 5.7b.

Target	e_p (mm)		e_v (°)	
	Mean	Std. Dev.	Mean	Std. Dev.
1	1,07	0,30	0,76	0,57
2	1,20	0,44	0,76	0,56
3	1,36	0,55	0,78	0,45
4	1,43	0,48	0,79	0,46
5	1,68	0,39	0,78	0,53
6	1,35	0,47	0,77	0,46
7	1,35	0,39	0,78	0,55
8	1,27	0,43	0,76	0,53
9	1,16	0,47	0,79	0,53
10	1,37	0,31	0,79	0,46
Mean	1,32	0,21	0,78	0,50

Table 5.10: Curvature-based registration accuracy.

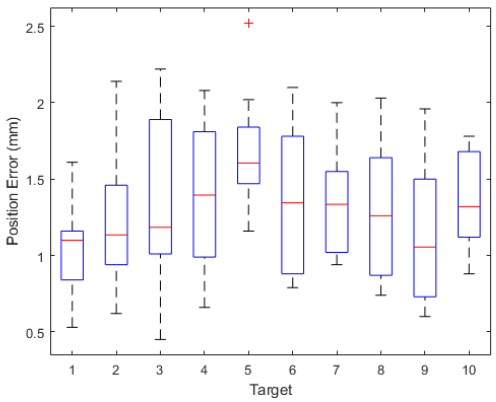

(a) Position error

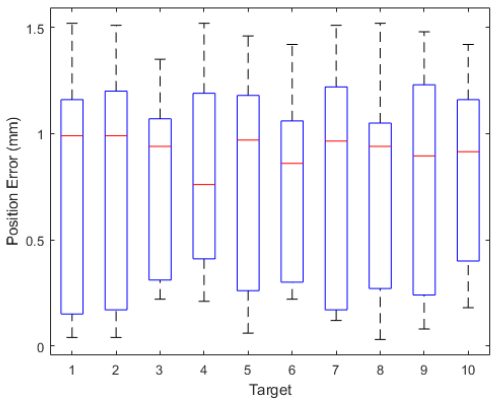

(b) Orientation error

Figure 5.7: Curvature-based registration target error distribution.

Finally, the processing time was calculated for every algorithm involved in the registration stage. The

Experiment	Processing Time (s)		
	US segmentation	PCA + ICP	Curvature-Based
1	23,64	1,25	33,37
2	23,38	1,72	35,73
3	17,32	0,90	42,96
4	22,27	1,53	45,39
5	19,16	1,80	28,50
6	17,98	1,08	28,76
7	25,48	4,93	29,46
8	26,47	1,28	33,10
9	19,73	1,30	51,66
10	24,61	0,83	29,71
Mean	22,04	1,66	35,86

Table 5.11: Processing time.

results are shown in table 5.11. For the ultrasound segmentation, the time presented is the total time that the algorithm took to segment all the images acquired, while the time present for the registration algorithms is the total time that these took to converge. Since the CT segmentation is not performed during the surgery, it will never be a bottleneck to the procedure, for that reason its processing time was not be evaluated. Some graphical results regarding the registration stage, i.e., the registered point clouds and targets, can be seen in appendix A.

Discussion

In what concerns the determination of $T_{CT}^{'Base}$, table 5.6 present a mean residue of 0.61 mm. This represents the minimum mean error that is possible to obtain in every registration step that involves both the CT information and the physical space information and there are two main factors behind this value.

The first is the CT resolution. It is shown in section 3.2.1 that this is around 0.5 mm along the X and Y axes and around 1 mm along the Z axis. On the other hand, it was already discussed that every position measured with the stylus is not perfectly accurate.

An imperfect choice of the CT segmentation threshold adds up to the aforementioned facts causing the relative position between the targets and the phantom surface to be different in the CT and in the physical space. As a consequence, the transformation that best aligns the surfaces is different from the one that best aligns the targets, figure 5.8. Thus, a mean position error of 0.85 mm and a mean orientation error of 0.14°result from the CT to ground truth registration, table 5.7.

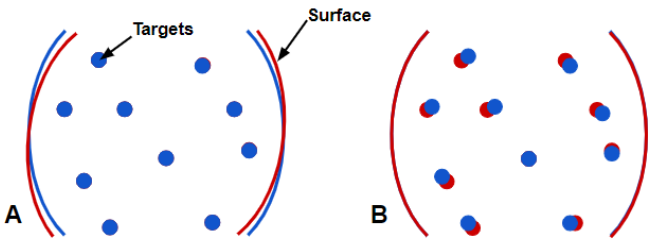

Figure 5.8: Registration top view in 2D. In A the targets perfect alignment results in a slight misalignment of the surfaces. By aligning the surfaces in B the targets get misaligned.

Regarding the registration steps involving the ultrasound imaging, 10 different ultrasound scans were

made. In section 3.5, one referred that the ultrasound and the stylus surfaces were expected to not overlap perfectly. The error introduced by this mismatch was measured by the ultrasound to ground truth registration and resulted in a mean position error of 0.66 mm and a mean orientation error of 0.4°. This result is mainly related to the flawed ultrasound spatial calibration and Polaris to robot calibration, both presented and discussed in the previous section. Also, as mentioned for the CT, the ambiguous choice of the ultrasound segmentation threshold, adds up for these errors.

An additional potential source of error is related to the phantom surface scanning. Whenever the transducer is not completely perpendicular to the surface the specular reflection and the ultrasound wave diffraction, figure 5.9, will degrade the image. This degradation can be more or less significant but will cause the image segmentation to result in a poorer surface. It is important to mention that this phenomena are strongly correlated to each specific ultrasound scan performed, being the main reason behind the decision of performing 10 independent experiments.

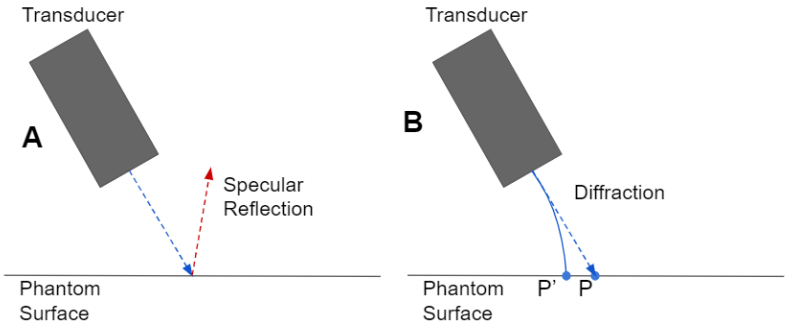

Figure 5.9: Image degradation due to non-perpendicular imaging. In A the specular reflection causes the surface to appear less brighter in the image. In B the diffraction causes the point P' to be imaged instead of P.

A final concern was related to the phantom displacement throughout the procedure. A tracker was attached to it so that this movement could be measured. Table 5.12 shows the difference in the phantom initial and final position and shows that this was not a significant source of error.

Phantom Displacement	
d_x (mm)	0,093
d_y (mm)	0,006
d_z (mm)	0,080

Table 5.12: Phantom displacement throughout procedure measured in the Polaris reference frame.

Finally, the CT to ultrasound registration was performed. The first approach was to use the PCA + ICP which resulted in a mean position error of 4.46 mm and a mean orientation error of 4.87°, table 5.9. These are large errors, specially when compared to the ones obtained in the previous two steps, and are related to the algorithm capability to solve the problem. Consequently, a more detailed analysis is needed to find the source of this error. To start with, the PCA was applied with no further fine tuning and resulted in a mean position error of 13.47 mm and a mean orientation error of 9.95°over the 10 experiments. Also figures 5.10a and 5.10b show an example of the relative position between the two

point clouds after this initial coarse alignment step. Even though the target errors are high, by looking at the figures one can conclude that this is a suitable initial coarse alignment.

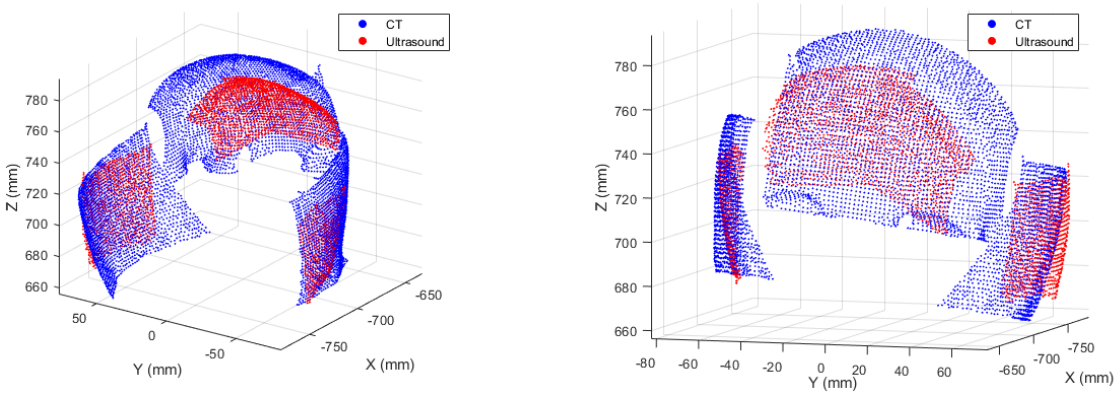

(a) (b)

Figure 5.10: Principal component analysis coarse registration.

The next approach was to apply the ICP over an initial alignment with the ground truth transformation, $T_{CT}^{\prime Base}$, to verify how the ICP would perform when it is given the best initial alignment possible. The results obtained can be seen in table 5.13.

Targets	e_p (mm)		e_v (°)	
	Mean	Std. Dev.	Mean	Std. Dev.
1	1,45	0,45	0,89	0,40
2	1,67	0,53	0,87	0,40
3	1,30	0,53	0,95	0,35
4	1,93	0,67	0,63	0,40
5	1,41	0,30	0,91	0,39
6	1,69	0,77	0,96	0,32
7	1,69	0,77	0,83	0,39
8	1,32	0,43	0,96	0,36
9	0,92	0,47	0,82	0,40
10	1,31	0,22	0,96	0,38
Mean	1,47	0,43	0,88	0,37

Table 5.13: ICP over $T_{CT}^{\prime Base}$ results.

Obviously, this is an unrealistic scenario, but one can observe that ICP results have improved a lot. It is possible to conclude that the better the initial alignment, the more accurate the ICP results are. On the other hand, it is relevant to analyse the ICP optimization residues in both cases, i.e., when it is applied after the PCA and the results are poor and when it is applied after the ground truth transformation and the results are much more satisfactory. The mean residue over the 10 ultrasound acquisitions was 1.04 mm for the first case and 0.97 mm for the second, that is, a decrease of 67 % in the mean target position error resulted in a 7 % decrease in the registration residue. There are two conclusions that can be taken. The first is that the ICP optimization criterion, i.e., the euclidean distance between the closest points, is not good enough to solve this problem, as it does not faithfully reflect the registration quality. The second is that the ICP ability to find a global minimum is poor and it often converges to the local minimum that is closer to the initial conditions.

The use of the mean and Gauss curvatures came up as a way to increase the amount of information available to perform the registration. Also, by using the shape of the cloud, which obviously does not depend on the cloud position, the initial conditions will no longer affect the registration outcome. It is important to refer that the mean position error of 1.32 mm and the mean orientation error of 0.78°, presented in table 5.10, are the result of every source of error described for the previous two steps. However, by looking at figures 4.37 and 4.38 it is possible to verify that the curvature estimation is not perfectly coherent in ultrasound and CT clouds which lead to the conclusion that the algorithm itself introduces an additional source of inaccuracy.

In what concerns, the processing time of the registration algorithms, the major reason behind the huge difference between the results in table 5.11 is that, for the ICP, the Matlab built-in function was used. This means that the time consuming part of the PCA+ICP algorithm was performed by compiled code. Differently, the curvature-based registration was fully implemented in Matlab meaning that the whole process was performed by interpreted code. Nevertheless, a considerable effort was put into reducing its processing time, for example by vectorizing the code and using built-in functions whenever it was possible.

5.3 Needle Placement

Results Presentation

The results for the first needle placement experiment, section 3.5, can be seen in table 5.14. It is important to refer that there are no results for the targets 5, 9 and 10 because these were not reachable by the robot in the used layout.

Target	e_p (mm)	e_v (°)
1	0,33	0,11
2	0,94	0,27
3	0,57	0,14
4	1,04	0,40
5	—	—
6	0,45	0,13
7	0,45	0,17
8	0,93	0,19
9	—	—
10	—	—
Mean	0,57	0,17

Table 5.14: Needle placement results using the targets measurement.

Since this experiments were performed in a different day, a new CT to ultrasound registration was performed. The result of the such registration can be seen in table 5.15a. Then, the robot was commanded using the registered CT. The results can be seen in figure 5.15b.

Target	e_p (mm)	e_v (°)
1	1,72	0,80
2	0,88	0,80
3	0,97	0,65
4	1,41	0,81
5	1,34	0,80
6	1,20	0,68
7	1,15	0,80
8	0,90	0,80
9	1,42	0,81
10	1,18	0,86
Mean	1,19	0,80

(a) Registration results.

Target	e_p (mm)	e_v (°)
1	1,90	0,94
2	1,47	1,01
3	1,26	0,65
4	2,51	1,19
5	—	—
6	1.88	0,76
7	1,39	0,91
8	0,56	0,84
9	—	—
10	—	—
Mean	1,43	0,91

(b) Needle placement results.

Table 5.15: Needle placement final results.

Discussion

The most prominent source of error behind the results of table 5.14 is related to the non-rigid phenomena described and discussed in section 5.1. Note that the needle to flange coordinate transformation was estimated through equation 4.10, which, in turn, uses the Polaris to robot base transformation. Consequently, the coupling base deflection causes the needle to flange coordinate transformation to be different depending on the configuration of the robot at the moment of the calibration. On the other hand, in the needle placing stage, each target demands a different robot configuration. It is then to be expected that the targets which demand a robot configuration most similar to the one used to calibrate, are the ones that present the lowest errors.

A simple procedure was performed to verify the validity of the proposed justification. This consisted in commanding the robot to move from the calibration configuration to the configuration demanded by each target. Similarly to the straight line experiment presented in section 5.1, the flange was tracked by the Polaris, and the magnitude of the non-rigid effects was measured through equation 5.1. The results can be seen in table 5.16.

Target	$d_{nonrigid}$ (mm)
1	0,05
2	0,39
3	0,08
4	0,69
6	0,32
7	0,11
8	0,47

Table 5.16: Non-rigid effects.

It is possible to verify that there is a clear trend between the results in table 5.14 and the values in table 5.16, which validates the justification provided.

An additional source of error as to do with the targets acquisition. These were acquired in the Polaris reference frame, using the stylus, and then transformed to the robot base reference frame, using the Polaris to robot transformation matrix. This has a mean error of 0.4 mm and therefore, the position of

the targets with reference to the robot base is expected to be biased.

Regarding the results for the registration presented in table 5.15a, these were obtained using the curvature-based algorithm. There is not further to add about them as the registration was already discussed in the previous section.

Finally in what concerns the results presented in table 5.15b, the biggest contribution comes, obviously, from the registration outcome. However, table 5.17 shows the robot isolated contribution to these final results. Δ_{ep} and Δ_{ev} correspond to the subtraction of the results in table 5.15a to the results in table 5.15b for both the position and the orientation errors, respectively.

Target	Δ_{ep} (mm)	Δ_{ev} (°)
1	0,18	0,14
2	0,59	0,21
3	0,29	0
4	1,1	0,38
6	0,68	0,08
7	0,24	0,11
8	-0,34	0,04

Table 5.17: Robot contribution to the final results.

It is interesting to note that, once again, there is a clear trend between the values in table 5.17 and the ones in table 5.16. This fact leads to the conclusion that the justification provided at the beginning of this section is indeed the most important source of error associated to the needle positioning stage as it was performed in the laboratory.

Chapter 6

Conclusions

Throughout the development of this thesis, the implementation of a robot-assisted and ultrasound-guided neuronavigation system was studied with regard to the image-to-patient registration and robot positioning.

Starting by the ultrasound calibration, although the issues reported in calibration results discussion, the variation proposed in the present work resulted in a PRA of 0.89 mm and a mean CR of 0.54 mm which, when compared to the results reported in [44], represent a significant improvement.

Regarding the Polaris to robot calibration, although the low mean error of 0.4 mm obtained, Tovar-Arriaga et al. [42] reports a mean error associated with the robot to the navigation system calibration of 0.23 mm, that is, around 43 % less than the error reported in the present work. This shows that a considerable progression margin exists in this step.

As for the segmentation algorithms and starting by the CT, segmenting the phantom CT images was a pretty straightforward task as this imaging modality does not present noise or artifacts of other kind. On the other hand, the segmentation of the ultrasound images required a little more effort so to produce a point cloud with no outliers. In both cases, the transition to a biological subject does not represent a substantial problem as the bone is a very noticeable feature in both imaging modalities.

The point cloud registration was tackled with two different approaches. A curvature-based algorithm was developed and compared against the widely used ICP with an initial coarse alignment step performed by the Principal Component Analysis. It was possible to verify that the proposed algorithm outperforms the ICP by 70 % in the targets position evaluation and by 84 % in the targets orientation evaluation. Furthermore, the results regarding the standard deviation of both the target position and orientation errors, reinforce the higher robustness of the curvature-based algorithm. Moreover, by evaluating the CT to ground truth and the ultrasound to ground truth registration steps, it is possible to conclude that the amount of error added by the algorithm is very low. This leads to the conclusion that the final error obtained in the registration stage is very close to the minimum achievable with the available hardware.

When compared with the literature, the final registration performance achieved in this work is only beaten by the screwed fiducials method which presents a minimum TRE of 0.7 mm in [23] and of 1

mm in [21]. However, this solution has several drawbacks, section 2.2.3, that are eliminated by the ultrasound-based registration. On the other hand, when compared with the non-invasive techniques, only the Z-touch is comparable to the proposed solution, presenting a minimum reported TRE of 1 mm, [22], in an arguably unrealistic study, section 2.2.4.

Regarding the needle positioning results, by comparing this with the mechanical execution error, performed with the Vertek articulating arm, reported in [24], one can verify that the error obtained with a robotic system is around 64 % less. Moreover, it is comparable the most accurate results achieved with the robotic systems available.

To finish, the needle positioning experiment presented in this work revealed that the deflection of the coupling base is a significant problem. By looking at tables 5.16 and 5.17, it is possible to verify that the robot contribution to the final error is very low in the targets to which the non-rigid effects are also low, which is a very promising result. This is what happens in targets 1, 3 and 7. However, it is also possible to verify that the maximum error obtained, target 4, resulted directly from this effect and strongly reduces the system's reliability. Therefore, it is crucial to solve this issue.

Finally, in what concerns the processing times presented in table 5.11 and starting by the segmentation, the mean result obtained over the 10 experiments was 22.04 s. This is the computational time that the algorithm took to process every image in the *.mha* file. Each file contained around 1900 to 2000 images which means that the time to process each image was around 0.012 s and thus, the algorithm processing rate is around 83 images per second. Given that the frame rate of the frame grabber is only 25 images per second, in a real application, the segmentation can be performed in real time and thus will not be a bottleneck to the surgical procedure. As for the processing time obtained with the proposed registration solution, the mean value of 35.86 s obtained is a bottleneck to the surgery procedure. As no task can be done in parallel, the surgeons and the patient would be just waiting, which may not be acceptable for a real case implementation. However, the implementation in a compiled language and the use of an high performance workstation are surely enough to solve this issue.

6.1 Achievements

It is worth stressing out, as main achievements of the present thesis, the following:

- The design, implementation and validation of an easy, automatic and accurate setup calibration procedure.
- The design, implementation and validation of a rigid registration mathematical framework that outperforms the most widely used algorithms by a considerably high margin.
- The design of a stepwise error evaluation methodology that can be used to evaluate any robot-assisted and ultrasound-guided neuronavigation system.
- A practical study with KUKA LBR Med in the Surgical Robotics Laboratory that can be used to guide further developments on this project, setting the most important future goals.

- A final registration stage performance that is comparable to the most accurate systems available, using a non-invasive and affordable technology.

6.2 Future Work

It is one's belief that the main developments to allow the system to be implemented in a real surgical environment, are the following:

- To exchange the coupling base for a stiffer one and repeat the entire procedure. The displacement caused by the base deflection should not be more than 0.1 mm so that its influence is negligible.
- To study and evaluate the MRI to CT registration. In a real application, the target points are selected in the MRI image instead of the CT. For that reason, this registration error has a major importance.
- Repeat the entire procedure selecting the target points in the MRI and evaluate the total final accuracy.
- Apply the developed procedure with a setup more similar to a real surgical environment. For instance, using a biological subject, the Mayfield clamp and a realistic relative position between the robot and the subject.
- The development of every piece of hardware needed for a real implementation. That is, the integration of safety features like an emergency stop button and the enabling switches, and the integration of a precise tool exchanger for the robot flange.
- The implementation of the registration and segmentation algorithms in a compiled language to decrease their processing time.
- The development of a suitable guided user interface to aid all the surgical procedures.

Bibliography

[1] M. Elyseu. Registo Intraoperatório com Recurso a Ultrassons em Neurocirurgia. Master's thesis, Instituto Superior Técnico, 2018.

[2] J. Ferreira. Ultrasound-CT Registration in Image-Guided Pedicle Screw Placement. Master's thesis, Instituto Superior Técnico, 2019.

[3] P. Pires. *Position and Force Control of Lightweight Robot Manipulators for Orthopedic Surgery*. PhD thesis, Instituto Superior Técnico, 2014.

[4] J. Oliveira. Robotic Navigation System for Needle Positioning in Neurosurgery. Master's thesis, Instituto Superior Técnico, 2019.

[5] PRECISION. `https://www.precisionhealth.com.au/healthcare-services/advanced-neurosurgery-spinal-surgery/procedures-and-surgery/stereotactic-biopsy/`, Visited in December 2020.

[6] A. Compston. THE STRUCTURE AND FUNCTIONS OF CEREBELLUM EXAMINED BY A NEW METHOD. By Sir Victor Horsley. *Brain 130(6):1449-1452*, 2007.

[7] Elekta. `https://www.ama-assn.org/specialty/neurological-surgery-specialty-description`, Visited in November 2020.

[8] G. C. Ribas. Das trepanações pré-históricas à neuronavegação: evolução histórica das contribuições da neuroanatomia e das técnicas de neuroimagem à prática neurocirúrgica. *Arquivos Brasileiros de Neurocirurgia Brazilian Neurosurgery 25(04):166-175*, 2006.

[9] intamed. `https://intamed.co.za/modified-skull-clamp/`, Visited in November 2020.

[10] J. A. Parra, M. Carnalla, J. C. F. Vazquez, C. Osvaldo, and P. Guadarrama-Ortíz. Neuronavigation: imaging-guided Neurosurgery. *Revista Mexicana de Neurociencia 19(4):83-93*, 2018.

[11] C. Dorfer, H. Stefanits, E. Pataraia, S. Wolfsberger, M. Feucht, C. Baumgartner, and T. Czech. Frameless Stereotactic Drilling for Placement of Depth Electrodes in Refractory Epilepsy: Operative Technique and Initial Experience. *Operative Neurosurgery, Volume 10*, 2014.

[12] A. Dogra and M. Patterh. CT and MRI Brain Images Registration for Clinical Applications. *Journal of Cancer Science and Therapy 6(1):18-26*, 2014.

[13] S. Roy, A. Carass, A. Jog, J. Prince, and J. Lee. MR to CT Registration of Brains using Image Synthesis. *Proceedings of SPIE - The International Society for Optical Engineering 9034*, 2014.

[14] P. Willems, J. W. Berkelbach van der Sprenkel, C. A. F. Tulleken, M. A. Viergever, and M. J. B. Taphoorn. Neuronavigation and surgery of intracerebral tumours. *Journal of Neurology 253: 1123–1136*, 2006.

[15] G. Eggers, J. Mühling, and R. Marmulla. Image-to-patient registration techniques in head surgery. *International Journal of Oral and Maxillofacial Surgery 35(12):1081-95*, 2007.

[16] J. L. Herring and B. M. Dawant. Automatic Lumbar Vertebral Identification Using Surface-Based Registration. *Journal of Biomedical Informatics 34, 74–84*, 2001.

[17] Brainlab. `https://www.brainlab.com/surgery-products/overview-neurosurgery-products/cranial-navigation/#/`, Visited in November 2020.

[18] Z. Fanti, F. Torres, E. Hazan-Lasri, A. Gastelum-Strozzi, L. Ruiz-Huerta, A. Caballero-Ruiz, and F. A. Cosío. Improved Surface-Based Registration of CT and Intraoperative 3D Ultrasound of Bones. *Journal of Healthcare Engineering 2018(345):1-11*, 2018.

[19] D. V. Amin, T. Kanade, A. M. DiGioia, and B. Jaramaz. Ultrasound Registration of the Bone Surface for Surgical Navigation. *Computer Aided Surgery 8(1):1-16*, 2003.

[20] J. M. Fitzpatrick, J. B. WestJay, B. West, and C. R. Maurer Jr. Predicting error in rigid-body point-based registration. *IEEE Transactions on Medical Imaging 17(5):694 - 702*, 1998.

[21] E. B. Strong, A. Rafii, B. Holhweg-Majert, S. C. Fuller, and M. C. Metzger. Comparison of 3 Optical Navigation Systems for Computer-Aided Maxillofacial Surgery. *Archives of otolaryngology–head neck surgery 134(10):1080-4*, 2008.

[22] H.-T. Lübbers, P. Messmer, J. A. Obwegeser, R. A. Zwahlen, R. Kikinis, K. W. Grätz, and F. Matthews. Comparison of different registration methods for surgical navigation in cranio-maxillofacial surgery. *Journal of Cranio-Maxillofacial Surgery 36(2):109-16*, 2008.

[23] L. Stieglitz, J. Fichtner, R. H. Andres, P. Schucht, A.-K. Krähenbühl, A. Raabe, and J. Beck. The Silent Loss of Neuronavigation Accuracy: A Systematic Retrospective Analysis of Factors Influencing the Mismatch of Frameless Stereotactic Systems in Cranial Neurosurgery. *Neurosurgery 72(5)*, 2013.

[24] P. D. Batista, I. Machado, P. Roios, J. P. Lavrador, M. B. Cattoni, J. Martins, and H. Carvalho. Position and Orientation Errors in a Neuronavigation Procedure: A Stepwise Protocol Using a Cranial Phantom. *World Neurosurgery 126*, 2019.

[25] N. Nathoo, M. C. Cavuşoğlu, M. A. Vogelbaum, and G. H. Barnett. In Touch with Robotics: Neurosurgery for the Future. *Neurosurgery 56(3):421-33; discussion 421-33*, 2005.

[26] Renishaw. https://www.renishaw.com/en/neuromate-robotic-system-for-stereotactic-neurosurgery--10712, Visited in November 2020.

[27] ZIMMER BIOMET. https://www.zimmerbiomet.com/medical-professionals/cmf/rosa-brain.html, Visited in December 2020.

[28] N. J. Brandmeir, S. Savaliya, P. Rohatgi, and M. Sather. The comparative accuracy of the rosa stereotactic robot across a wide range of clinical applications and registration techniques. *Journal of Robotic Surgery 12(1)*, 2018.

[29] T. R. K. Varma and P. Eldridge. Use of the NeuroMate stereotactic robot in a frameless mode for functional neurosurgery. *The International Journal of Medical Robotics and Computer Assisted Surgery, 2(2):107–113*, 2006.

[30] Radiology Key. https://radiologykey.com/ultrasonic-systems/, Visited in November 2020.

[31] W. R. Hendee and E. R. Ritenour. *Medical Imaging Physics*, chapter 15. Wiley-Liss, 2002.

[32] W. R. Hendee and E. R. Ritenour. *Medical Imaging Physics*, chapter 19. Wiley-Liss, 2002.

[33] P. Teodoro. *Robust Surface Reconstruction and US Bone Registration for Hip Resurfacing Surgery*. PhD thesis, Instituto Superior Técnico, 2015.

[34] *KUKA Sunrise.OS Med 1.15, KUKA Sunrise.Workbench Med 1.15*. KUKA, 2018.

[35] A. D. Wiles, D. G. Thompson, and D. D. Frantza. Accuracy assessment and interpretation for optical tracking systems. *Proceedings of SPIE - The International Society for Optical Engineering 5367*, 2004.

[36] J. Tokuda, G. S. Fischer, X. Papademetris, Z. Yaniv, L. Ibanez, P. Cheng, H. Liu, J. Blevins, J. Arata, A. J. Golby, T. Kapur, S. Pieper, E. C. Burdette, G. Fichtinger, C. M. Tempany, and N. Hata. Openigtlink: an open network protocol for image-guided therapy environment. *International Journal of Medical Robotics and Computer Assisted Surgery 5(4):423-34*, 2009.

[37] A. Lasso, T. Heffter, A. Rankin, C. Pinter, T. Ungi, and G. Fichtinger. Plus: open-source toolkit for ultrasound-guided intervention systems. *IEEE transactions on bio-medical engineering*, 2011.

[38] L. Bartha, A. Lasso, C. Pinter, T. Ungi, Z. Keri, and G. Fichtinger. Open-source surface mesh-based ultrasound-guided spinal intervention simulator. *International Journal of Computer Assisted Radiology and Surgery 8(6)*, 2013.

[39] S. Pieper, M. Halle, and R. Hikinis. 3D Slicer. *IEEE International Symposium on Biomedical Imaging*, 2004.

[40] B. Hallgrímsson and C. W. Sensen. *Advanced Imaging in Biology and Medicine*, chapter 3. Springer, 2009.

[41] E. M. Moult, A. Lasso, T. Ungi, C. Pinter, M. Welch, and G. Fichtinger. Improved Temporal Calibration of Tracked Ultrasound: An Open-Source Solution. *Journal of Medical Robotics Research 02(04):1-8*, 2017.

[42] S. Tovar-Arriaga, R. Tita, J. C. P. Ortega, E. Gorrostieta-Hurtado, and W. A. Kalender. Development of a robotic FD-CT-guided navigation system for needle placement-preliminary accuracy tests. *International Journal of Medical Robotics and Computer Assisted Surgery 7(2):225-36*, 2011.

[43] R. Prager, R. N. Rohling, A. H. Gee, and L. Berman. Rapid calibration for 3-D freehand ultrasound. *Ultrasound in Med. Biol., Vol. 24*, 1998.

[44] P.-W. Hsu, G. M. Greece, R. Prager, N. E. Houghton, and A. H. Gee. Comparison of Freehand 3-D Ultrasound Calibration Techniques Using a Stylus. *Ultrasound in Medicine Biology 34(10):1610-21*, 2008.

[45] P. J. Besl and N. D. McKay. A Method for Registration of 3-D Shapes. *IEEE Transactions on Pattern Analysis and Machine Intelligence 14(2):239-256*, 1992.

[46] S. Rusinkiewicz and M. Levoy. Efficient variants of the ICP algorithm. *Proceedings Third International Conference on 3-D Digital Imaging and Modeling*, 2001.

[47] H. Pottman, Q. Huang, Y.-L. Yang, and S.-M. Hu. Geometry and Convergence Analysis of Algorithms for Registration of 3D Shapes. *International Journal of Computer Vision 67(3):277-296*, 2006.

[48] Y. Liu. A mean field annealing approach to accurate free form shape matching. *Pattern Recognition 40(9):2418-2436*, 2007.

[49] M. H. Moghari and P. Abolmaesumi. Point-Based Rigid-Body Registration Using an Unscented Kalman Filter. *IEEE TRANSACTIONS ON MEDICAL IMAGING*, 2007.

[50] H. Talib, M. Peterhans, J. G. Giraldez, M. Styner, and M. Ballester. Kalman Filtering for Frame-by-Frame CT to Ultrasound Rigid Registration. *Medical Imaging and Augmented Reality*, 2008.

[51] A. Myronenko and X. Song. Point Set Registration: Coherent Point Drift. *IEEE Transactions on Software Engineering 32(12):2262-75*, 2010.

[52] Y. Liu, Z. Song, and M. Wang. A new robust markerless method for automatic image-to-patient registration in image-guided neurosurgery system. *Computer Assisted Surgery 22(sup1):1-7*, 2017.

[53] H. Tian, X. Dang, J. Wang, and D. Wu. Registration method for three-dimensional point cloud in rough and fine registrations based on principal component analysis and iterative closest point algorithm. *Traitement du Signal 34(1-2):57-75*, 2017.

[54] R. Echeverria-Chasco, C. Cortes, A. Bertelsen, and J. F. Esnal. Robust CT to US 3D-3D Registration by Using Principal Component Analysis and Kalman Filtering. *International Workshop on Computational Methods and Clinical Applications for Spine Imaging*, 2016.

[55] X. Zhang. Curvature estimation of 3d point cloud surfaces through the fitting of normal section curvatures. 2008.

[56] H. Hoppe, T. D. DeRose, T. Duchamp, J. A. McDonald, and W. Stuetzle. Surface reconstruction from unorganized points. *ACM SIGGRAPH Computer Graphics*, 1992.

[57] K. S. Arun, T. S. Huang, and S. D. Blostein. Least-squares fitting of two 3-D point sets. IEEE T Pattern Anal. *IEEE Transactions on Pattern Analysis and Machine Intelligence PAMI-9(5):698*, 1987.

Appendix A

Graphical Registration Results

This appendix aims to show some graphical results of the registration stage. Here both the targets and the point clouds final alignment obtained are shown for the US to CT registration.

The results for three scans will be shown. These are the cloud that produced the best results (Scan 1), the cloud that produced the worst results (Scan 2), and a randomly selected cloud for which the results are near the mean (Scan 3), for both the PCA+ICP and the curvature-based registration.

Notice that 10 independent scans were performed, however, it would be tiresome to present the results of all the 10 point clouds acquired for both algorithms. Besides, no further information would be added.

Having said so, figures A.1 to A.3 show the PCA+ICP results while figures A.4 to A.6 show the curvature-based results.

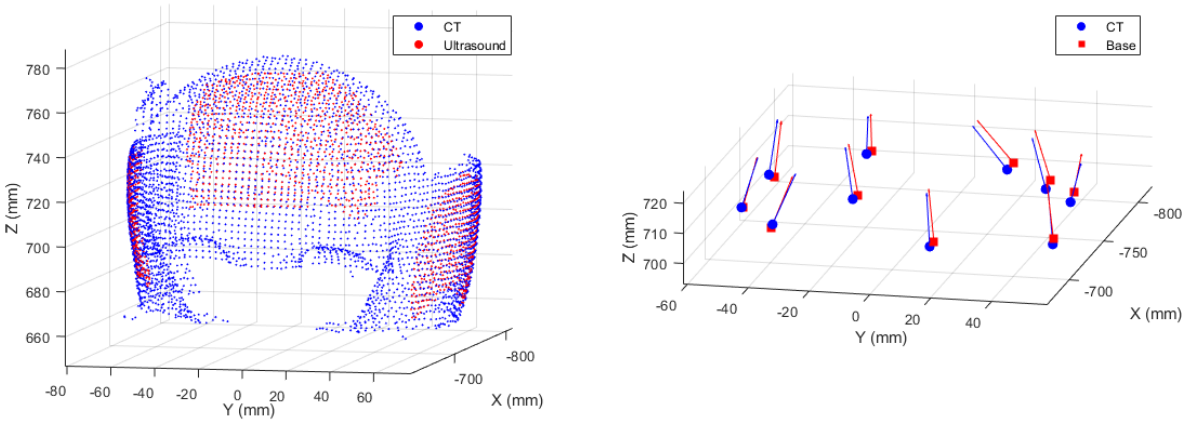

(a) Clouds

(b) Targets

Figure A.1: Scan 1. PCA+ICP registration: Mean $e_p = 2.51mm$; Mean $e_v = 2.38°$.

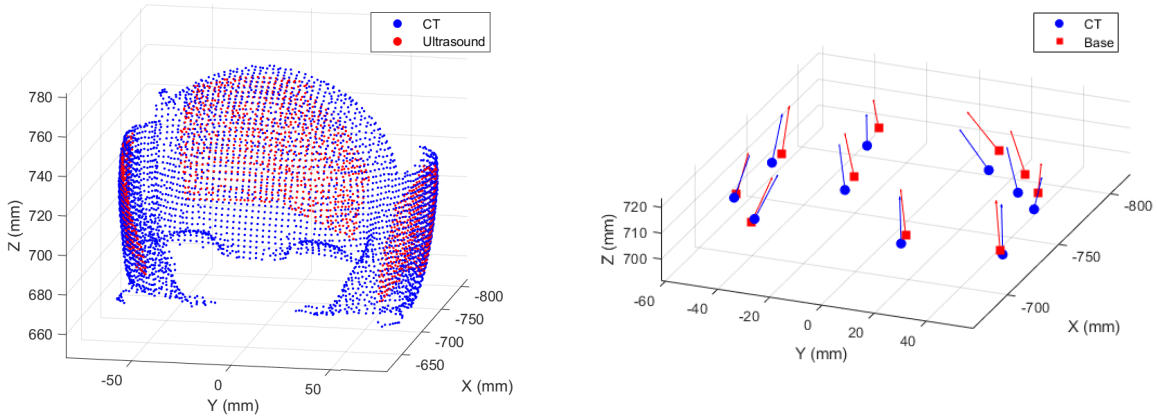

(a) Clouds (b) Targets

Figure A.2: Scan 2. PCA+ICP registration: Mean $e_p = 5.83mm$; Mean $e_v = 5.65°$.

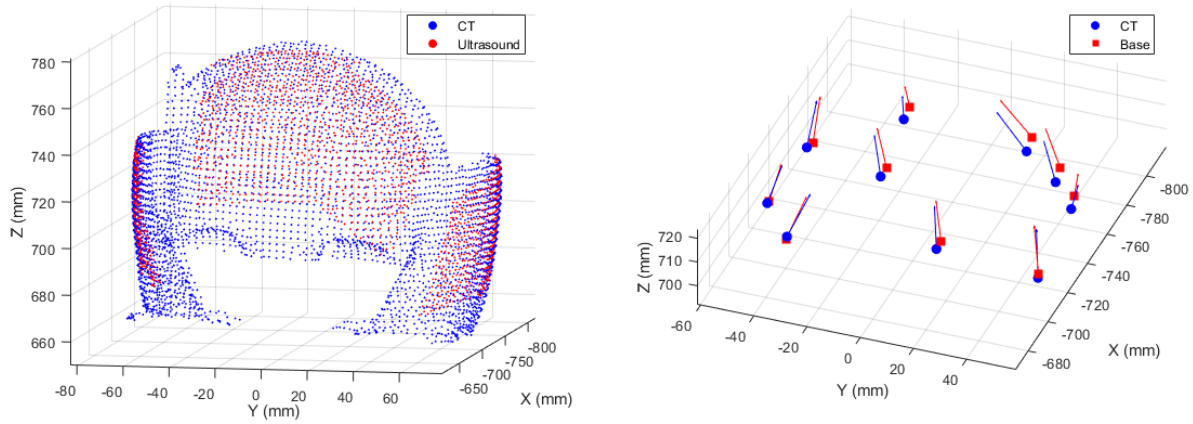

(a) Clouds (b) Targets

Figure A.3: Scan 3. PCA+ICP registration: Mean $e_p = 4.16mm$; Mean $e_v = 4.41°$.

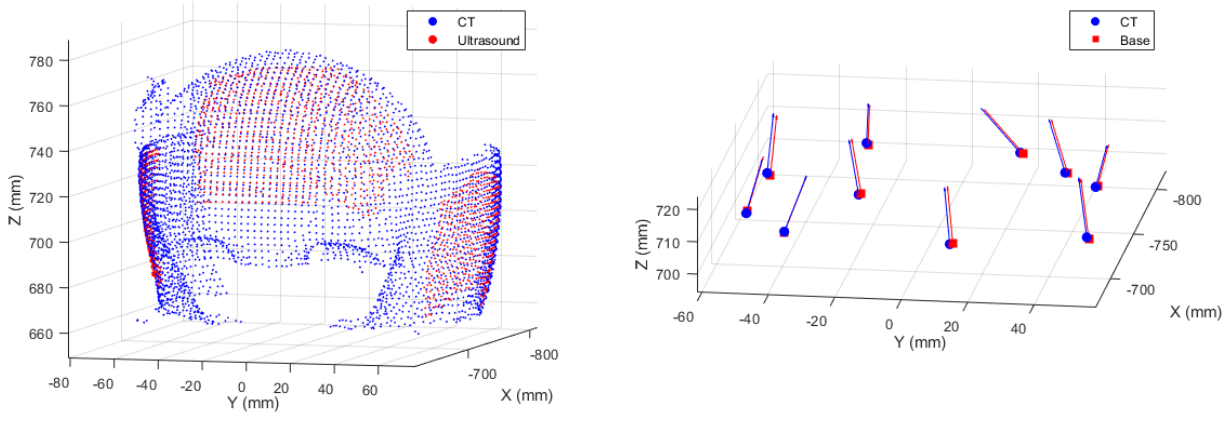

(a) Clouds (b) Targets

Figure A.4: Scan 1. Curvature-Based registration: Mean $e_p = 0.94mm$; Mean $e_v = 0.19°$.

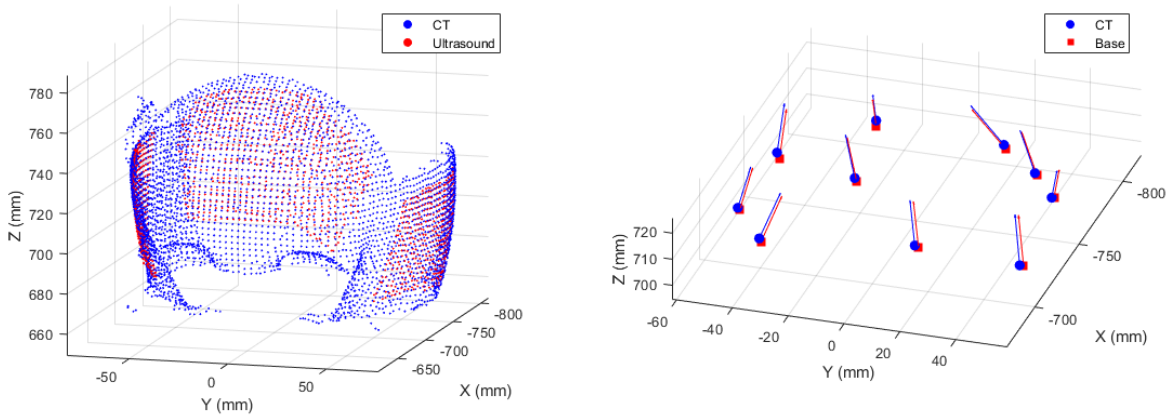

(a) Clouds (b) Targets

Figure A.5: Scan 2. Curvature-Based registration: Mean $e_p = 1.66mm$; Mean $e_v = 0.85°$.

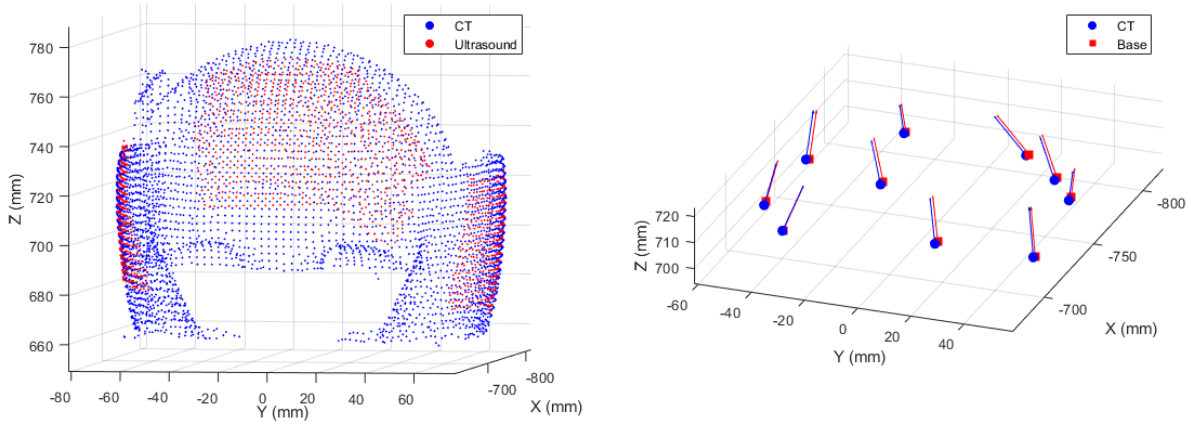

(a) Clouds (b) Targets

Figure A.6: Scan 3. Curvature-Based registration: Mean $e_p = 1.28mm$; Mean $e_v = 0.34°$.